Volume 6
Number 23
7 December 2024
Pages 5739–6030

Nanoscale Advances

rsc.li/nanoscale-advances

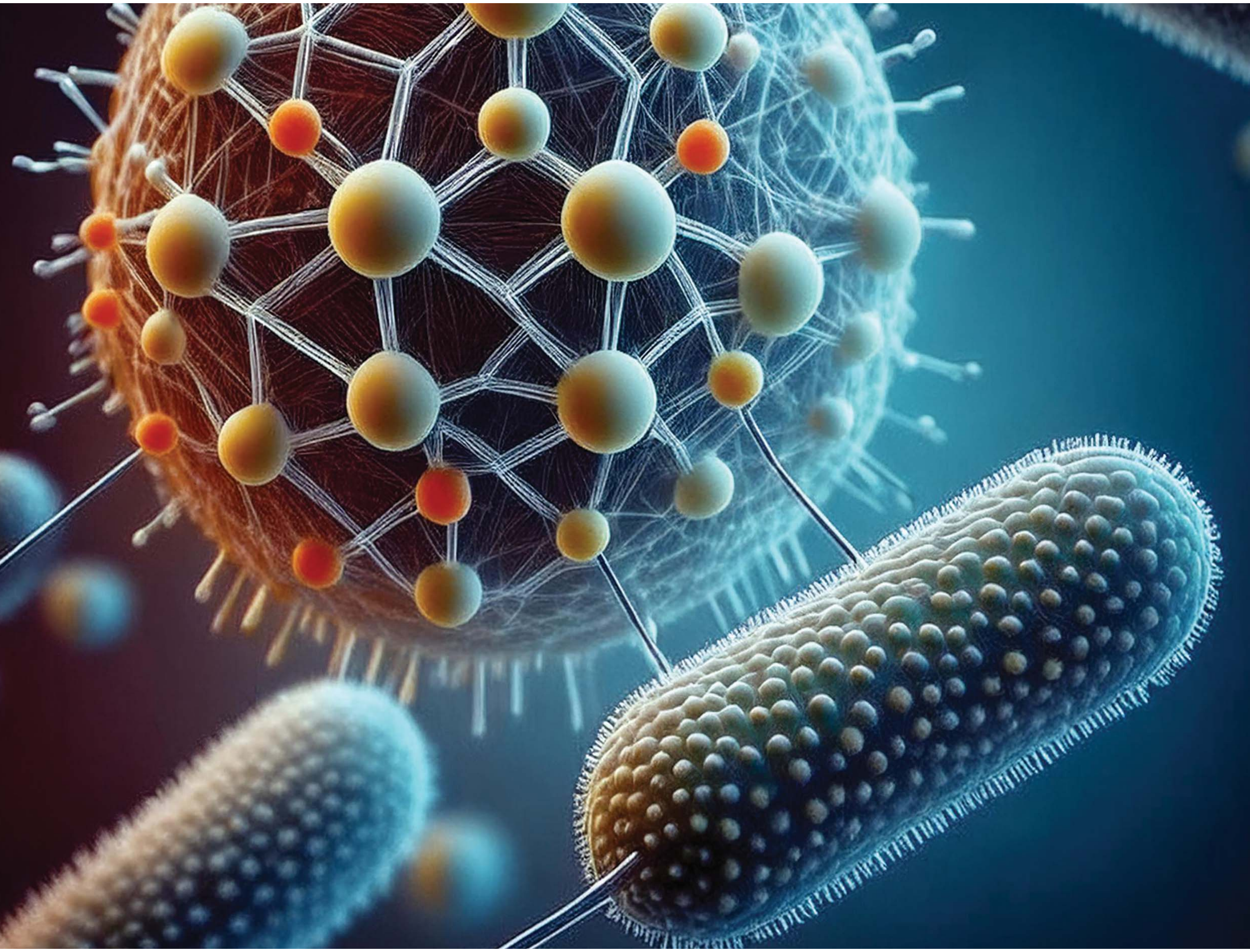

ISSN 2516-0230

ROYAL SOCIETY OF CHEMISTRY

PAPER
Sherine O. Obare, Anthony L. Dellinger *et al.*
A rapid one-step synthesis of silver and copper coordinated chlorine functionalized fullerene nanoparticles with enhanced antibacterial activity

NCNST

Nanoscale Advances

PAPER

View Article Online
View Journal | View Issue

Cite this: *Nanoscale Adv.*, 2024, **6**, 5833

A rapid one-step synthesis of silver and copper coordinated chlorine functionalized fullerene nanoparticles with enhanced antibacterial activity†

Abed Alqader Ibrahim,[a] Tariq Khan,[a] Kyle Nowlin,[a] Jared Averitt,[a] Gayani Pathiraja,[a] Dennis LaJeunesse,[a] Sherine O. Obare*[a] and Anthony L. Dellinger*[abc]

Received 2nd September 2024
Accepted 15th October 2024

DOI: 10.1039/d4na00732h

rsc.li/nanoscale-advances

Nanoparticle modification demonstrates a remarkable synergetic effect in combating bacteria, particularly resistant bacteria, enhancing their efficacy by simultaneously targeting multiple cellular pathways. This approach positions them as a potent solution against the growing challenge of antimicrobial-resistant (AMR) strains. This research presents an investigation into the synthesis, characterization, and antibacterial evaluation of silver-coordinated chloro-fullerenes nanoparticles (Ag-C_{60}-Cl) and copper-coordinated chloro-fullerenes nanoparticles (Cu-C_{60}-Cl). Utilizing an innovative, rapid one-step synthesis approach, the nanoparticles were rigorously characterized using X-ray Photoelectron Spectroscopy (XPS), Scanning Electron Microscopy-Energy Dispersive X-ray Spectrometer (SEM-EDS), High-Resolution Transmission Electron Microscopy (HR-TEM), Fourier-Transform Infrared Spectroscopy (FTIR), and Raman spectroscopy. In conjunction with the analytical techniques, a computational approach was utilized to corroborate the findings from Raman spectroscopy as well as the surface potential of these nanoparticles. Moreover, the antibacterial activities of the synthesized nanoparticles were assessed against *Escherichia coli* (*E. coli*) and Methicillin-Resistant *Staphylococcus aureus* (MRSA). These findings demonstrated that the synthesized Ag-C_{60}-Cl and Cu-C_{60}-Cl nanoparticles exhibited minimum inhibitory concentrations (MIC) of 3.9 μg mL^{-1} and 125 μg mL^{-1}, respectively. Reactive oxygen species (ROS) quantification, catalase assay, and efflux pump inhibition results revealed promising broad-spectrum antibacterial effects.

Introduction

Antimicrobial resistance (AMR) presents a significant challenge to global public health, resulting in 1.27 million mortalities worldwide and was associated with nearly 5 million deaths in 2019.[1] In the US, antibiotic resistance is present in more than 2.8 million infections each year.[2] Overprescription of antibiotics, their widespread use in agriculture, and the lack of new antibiotics have all contributed to the rapid development of AMR.[3,4] In the contemporary landscape of healthcare, where repeated drug administrations, escalated doses and a dearth of stewardship are commonplace, AMR has surfaced as a formidable challenge. This issue is particularly problematic and noticeable for a variety of antibiotic classes that have historically been effective in preventing infections caused by pathogenic microorganisms.[5] Nanomaterials excel as drug carriers due to their exceptional drug loading capacity, precision in controlled and targeted drug delivery, and enhanced drug bioactivity. These features position nanomaterials as an ideal platform for drug delivery, enabling controlled release of therapeutic agents and significantly enhancing their pharmacological effectiveness.[6–8]

The properties, behaviors, and potential utility of carbon-based nanomaterials, including carbon nanotubes, fullerenes, and graphene, have been extensively investigated for more than two decades. These materials have undergone comprehensive scrutiny, emerging as multifunctional materials with substantial potential in numerous biomedical applications.[9] Fullerene molecules, also known as buckyballs can exist in various arrangements, commonly including C_{60}, C_{70}, and other configurations where the number of carbon atoms ranges from 20 (C_{20}) to over 300. The surface of a C_{60} fullerene is distinguished by the arrangement of 20 hexagons and 12 pentagons, wherein all rings are intricately fused, and the double bonds display conjugation throughout the structure.[10] The C_{60} fullerenes have molecular stability and higher degree of symmetry compared to other fullerene molecules. The symmetry and consistent overall curvature of the C_{60} fullerene provides more

---

[a] *Department of Nanoscience, Joint School of Nanoscience and Nanoengineering, University of North Carolina at Greensboro, Greensboro, NC, 27401, USA. E-mail: aldellin@uncg.edu; soobare@uncg.edu*
[b] *Kepley Biosystems Incorporated, Greensboro, NC, 27214, USA*
[c] *AT Research Partners, Burlington, NC, 27217, USA*

† Electronic supplementary information (ESI) available. See DOI: https://doi.org/10.1039/d4na00732h

uniform properties and reactive sites which allow for greater control, uniformity and predictability during functionalization. In contrast, C_{70} fullerenes have a more prolate spheroid shape, where the reactivity and accessibility can vary between the molecular poles and equatorial regions.

Numerous studies have elucidated the potential biomedical applications of carbon-based nanomaterials, including their therapeutic efficacy in addressing neurodegenerative diseases, their role as inhibitors for nitric oxide synthase, and their capacity as agents for DNA cleavage.[11–13] These nanoparticles have also shown promise as drug carriers.[14]

Recent research has shown a growing interest in multifunctional antimicrobial composites, where the synergistic enhancement of antimicrobial characteristics is achieved through the combination of two independent components.[15] Studies have been conducted to clarify the implications of combining fullerenes with various metals such as silver,[16] gold,[17] and iron,[18] investigating the cooperative interactions and potential applications of these composites.

In a study by Brunet *et al.*, the role of reactive oxygen species (ROS) in the antibacterial activity of several photoactive nanomaterials were investigated using the model bacterium *Escherichia coli* (*E. coli*). Different types of fullerenes including aggregates, hydroxylated, and coated as well as nano-TiO_2 suspensions were evaluated. The results showed that both C_{60} fullerenes and TiO_2 nanoparticles exhibit strong antibacterial activity through ROS generation. While C_{60} fullerenes demonstrated comparable antibacterial effectiveness to TiO_2, they were more versatile, remaining effective under a broader range of light conditions, including visible light.[19,20] In other research, Kawasaki *et al.* demonstrated the effective elimination of bacteria *via* photodynamic activation of fullerene derivatives incorporated into liposome membranes.[21]

In this study, a rapid one-step procedure for synthesizing silver-coordinated chloro-fullerenes nanoparticles (Ag-C_{60}-Cl) and copper-coordinated chloro-fullerenes nanoparticles (Cu-C_{60}-Cl) was obtained. Ag-C_{60}-Cl and Cu-C_{60}-Cl over Ag-C_{60} and Cu-C_{60} were selected and evaluated to enhance the antibacterial activity of the nanoparticles. The incorporation of chlorine as functional groups increased surface reactivity, allowing for stronger interactions with bacterial membranes. Silver and copper were selected due to their well-established antimicrobial properties. The coordination of these metals with chlorinated fullerenes amplifies these effects, making them potent agents against Gram-positive and Gram-negative bacteria. The antibacterial activity of the nanoparticles was evaluated against *E. coli* and Methicillin-resistant *Staphylococcus aureus* (MRSA).

Experimental

One-step synthesis of Ag-C_{60}-Cl and Cu-C_{60}-Cl nanoparticles *via* a facile sonication-assisted method

The synthesis of Ag-C_{60}-Cl nanoparticles was conducted; accordingly, 5 mg of C_{60} fullerene (99.95+% SES research) was dissolved in 5 mL of chloroform (anhydrous, ≥99%, Sigma) and sonicated for 10 minutes using a bath sonicator. Subsequently, 2 mL of a 2 M $AgNO_3$ (ACS reagent, ≥99.0%, Sigma) solution was added dropwise to the C_{60} solution while continuously probe sonicated for an additional 10 minutes. The resulting mixture underwent centrifugation, followed by three washes with deionized water to remove any residual reactants as shown in Fig. 1. The obtained Ag-C_{60}-Cl nanoparticles were then dried for further testing.

The same procedure was employed for the preparation of Cu-C_{60}-Cl nanoparticles. In this synthesis, 5 mg of C_{60} fullerene was dissolved in 5 mL of chloroform and sonicated for 10 minutes. Following this, 2 mL of a 2 M Cu(II) nitrate (≥99.9% trace metals basis) solution was added dropwise to the C_{60} solution during probe sonication for an additional 10 minutes. The subsequent steps, including centrifugation, washing, and drying, mirrored those employed in the Ag-C_{60}-Cl synthesis.

Characterization

X-ray photoelectron spectroscopy (XPS). XPS was conducted on a Thermos Scientific™ K-Alpha™+ spectrometer equipped with a monochromatic Al Kα X-ray source (1,486.6 eV) operating at 100 W to obtain the elemental compositions. Samples were analyzed under vacuum ($P < 10^{-7}$ mbar) with a pass energy of 200 eV for survey scans or 30 eV for high-resolution scans. All peaks were calibrated with C 1s peak binding energy at 284.8 eV for adventitious carbon. Drop-casted samples on a Si wafer were used to obtain the micro elemental compositions and were matched with the XPS elemental survey analysis.

Scanning electron microscopy (SEM) and energy-dispersive X-ray spectroscopy (EDS). SEM/EDS analysis was performed to analyze nanoparticle morphologies using a JEOL JSM-IT800 FESEM with Oxford Ulti Max EDS. X-ray data was acquired at 15 kV in low vacuum mode with a chamber pressure of 50 Pa. Electron micrographs were generated utilizing a low vacuum backscattered electron detector (LVBED). The bacterial samples for SEM imaging were prepared using a modified fixation protocol based on standard procedures.[22] A glutaraldehyde-formaldehyde mixture (Karnovsky's fixative) was used for primary fixation to preserve cellular morphology. Briefly, the bacteria were treated with the nanoparticles at the MIC concentrations and incubated for 2–4 hours. The samples were rinsed several times in phosphate-buffered saline (PBS) to remove excess fixative and nanoparticles followed by immersing the samples with the fixation solution for 1–2 hours. The bacteria were then centrifuged and washed several times with 0.1 M cacodylate buffer, pH 7.4. A gradual dehydration series was performed using increasing concentrations of ethanol (35%, 50%, 95%, and 100%). Following the dehydration step, the bacterial suspension was deposited onto clean Si wafer for further imaging. Centrifugation was employed during the rinsing and dehydration steps to ensure proper pelleting of bacterial cells. A low-speed centrifugation (4000 RCF for 5 minutes at room temperature) was used to avoid potential damage to the bacterial cells.

Raman spectroscopy. Raman spectra were recorded on a Renishaw System 2000 (with an integral microscope) using excitation radiation at 514 nm from an Ar^+ ion laser (Spectraphysics model 236C).

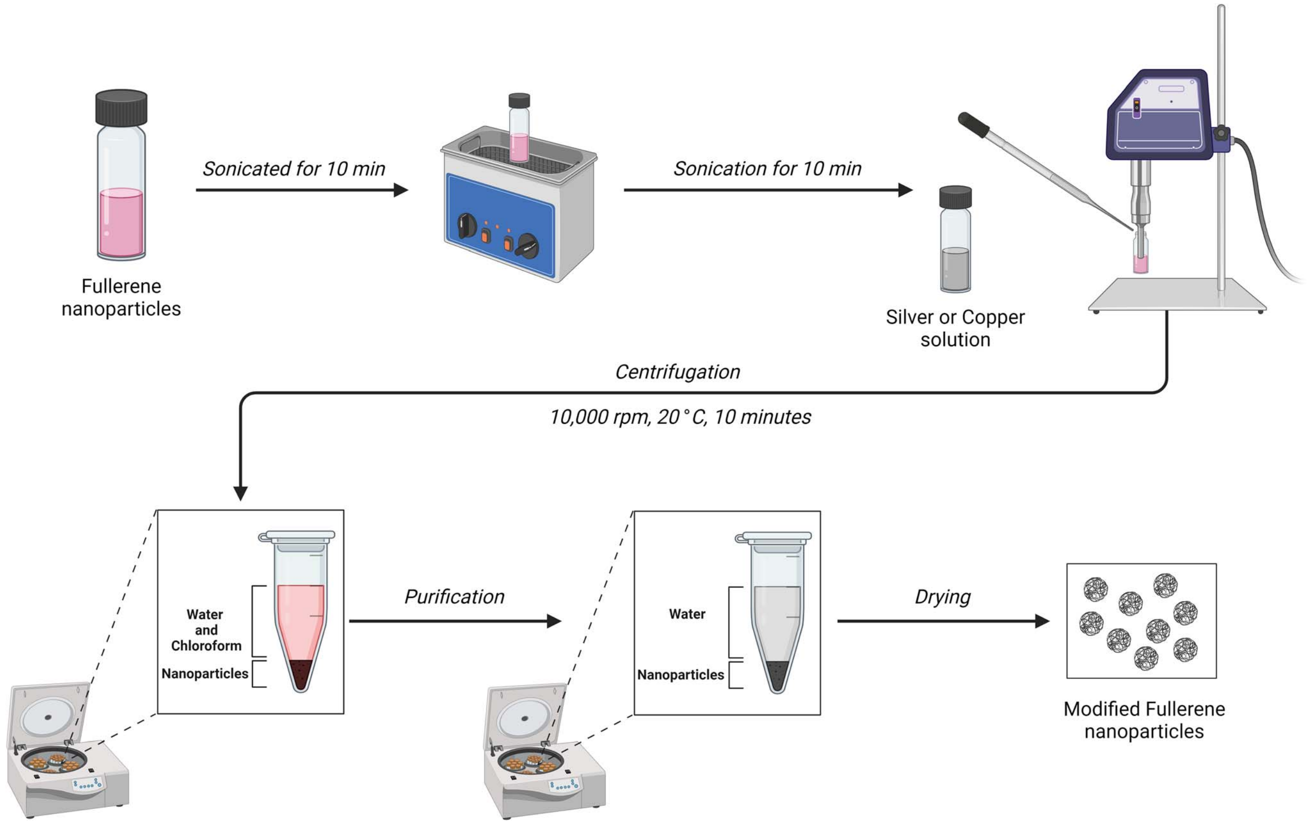

Fig. 1 Schematic representation for the synthesis of the nanoparticles.

Fourier-transform infrared spectroscopy (FTIR). FTIR spectra were obtained using an Agilent 670 FTIR Spectrometer w/ATR to further confirm the molecular functionalization. Samples were analyzed directly, with air used as the blank.

High-resolution transmission electron microscopy (HR-TEM). The high-resolution transmission electron microscopy (HR-TEM) operated at an accelerating voltage of 80 kV from JEOL 2100PLUS with a STEM/EDS capability was used to examine the morphology and crystallinity of nanostructures dispersed in deionized water.

Antimicrobial activity studies

All microbiological experiments were performed in triplicates, and the results are expressed as mean values with the standard error of the mean (SEM) included for statistical accuracy.

Disc diffusion assay

The disc diffusion method was used to evaluate the antimicrobial activity of Ag-C_{60}-Cl and Cu-C_{60}-Cl nanoparticles against wild-type *E. coli* (BW25113) and MRSA (BAA-1720). This method was performed in Luria–Bertani (LB) medium solid agar Petri dish. The discs were cut into a sterile Whatman No. 1 paper disc shape with a diameter of 6 mm, sterilized by autoclaving for 15 minutes at 70 °C and placed on *E. coli* cultured agar plate and MRSA cultured agar plate, loaded with 10 μL of different concentration of each of the nanoparticles and then incubated for 24 hours at 37 °C and the inhibition zones were monitored. After incubation, the presence of bacterial growth inhibition halo around the samples was absorbed, and their diameter in millimeters was measured.

Minimum inhibition concentration

The microdilution assay was used to determine the minimum inhibitory concentration (MIC) of C_{60}-Cl fullerenes, Ag-C_{60}-Cl, and Cu-C_{60}-Cl nanoparticles by evaluating the visible growth of microorganisms in broth media.[23] A series of two-fold dilutions of nanoparticles, ranging from 500 μg mL^{-1} to 0.9765 μg mL^{-1}, was prepared with an adjusted bacterial concentration (0.5 McFarland standard) in Brain Heart Infusion (BHI) broth within a 96-well plate. The control group contained only inoculated broth and was incubated for 24 hours at 37 °C. The MIC was determined as the lowest concentration of nanoparticles that showed no visible growth was observed in the wells. To validate the MIC value, the visual turbidity of the wells was noted both before and after incubation. Silver nitrate ($AgNO_3$) was used as a control. Its well-documented antimicrobial properties provide a benchmark for comparison and help validate the efficacy of the nanoparticles.[24–26]

Reactive oxygen species quantification

ROS level quantification was conducted according to the protocol by Pérez *et al.* protocol.[27] In brief, bacterial cells were exposed to varying concentrations of Ag-C_{60}-Cl, Cu-C_{60}-Cl, and C_{60}-Cl nanoparticles, utilizing the oxidant-sensitive probe,

H_2DCFDA. The bacterial cells were cultured in an LB medium until reaching an optical density (OD) of 0.5 at 600 nm. Subsequently, cells were harvested through centrifugation, washed with 10 mM potassium phosphate buffer (pH 7.0), and disrupted by sonication after suspension in the same buffer. The oxidant-sensitive probe H_2DCFDA, dissolved in dimethyl sulfoxide, was added to the cell suspension at a ratio of 1 : 2000, followed by a 30-minute incubation at 37 °C with shaking. After centrifugation to form a cell pellet, excess H_2DCFDA was removed through two washes with the same buffer. Cleaned cells suspended in buffer were then exposed to nanoparticles at concentrations ranging from 0.1–500 μg mL^{-1}. Finally, the fluorescence intensity of 2′,7′-dichlorofluorescein (DCF) was measured using a fluorescence spectrophotometer at an excitation wavelength of 488 nm and an emission wavelength of 535 nm. Hydrogen peroxide (H_2O_2) was used as a positive control to induce ROS production. H_2O_2 is a well-established oxidizing agent that causes oxidative stress in bacterial cells by generating ROS.

Catalase assay

To evaluate the catalase activity of the samples, the Amplex Red Catalase Assay was performed. The assay Amplex Red reagent stock solution was prepared by dissolving 0.26 mg of the reagent in 100 μL of DMSO (10 mM). A 1× Reaction Buffer was formulated by combining 4 mL of 5× Reaction Buffer stock with 16 mL deionized water. Additionally, a 100 U mL^{-1} HRP solution and a 20 mM H_2O_2 working solution were prepared. In parallel, a 1000 U mL^{-1} catalase solution was derived by dissolving catalase in 100 μL of deionized water. For the assay, samples were diluted in 1× Reaction Buffer and pipetted into a microplate. A 40 μM H_2O_2 solution was then added, followed by a 30-minute incubation. Subsequently, a working solution of 100 μM Amplex Red reagent with 0.4 U mL^{-1} HRP was prepared. In the second phase of the reaction, 50 μL of the Amplex Red/HRP working solution was added to each well containing samples with concentrations ranging from 7.8–500 μg mL^{-1}, along with appropriate controls. The plate was then incubated for a least 30 minutes at 37 °C, protected from light. Fluorescence was measured using a microplate reader with excitation in the 530–560 nm range and emission detection at approximately 590 nm. The change in fluorescence was determined by subtracting the sample value from that of the no-catalase control.

Efflux pump inhibition assay

To evaluate the efflux pump activity of *E. coli* and MRSA in the presence of fullerenes, a cartwheel assay was employed following a modified protocol by Christena *et al.*[28] This method was chosen to gauge the anti-resistance mechanisms of fullerenes. Briefly, Mueller Hinton agar plates were prepared with ethidium bromide (EtBr; 0.1 μg mL^{-1}). C_{60}-Cl, Ag-C_{60}-Cl, and Cu-C_{60}-Cl nanoparticles were added to media at 0.25× MIC concentrations, with tetracycline as the positive control and bacteria as negative control. Bacterial cultures, grown overnight, were adjusted to $OD_{600} = 0.5$ and swabbed onto Ethidium bromide-Mueller-Hinton-NPs (EtBr-MH-NPs) plates in a cartwheel pattern and held at 37 °C for 24 hours. After incubation, the plates were then examined under a UV transilluminator, and images were captured to compare the fluorescence intensity of the lines.

Results

Raman spectroscopy

The inherent binding characteristics of the nanoparticles synthesized through the liquid–liquid interfacial method were determined using a Raman survey, as depicted in Fig. 2. The Raman-active bands in C_{60} fullerene molecules exhibited a significant decay, mirroring observations made in hybrid microcrystals produced through liquid–liquid interfacial and solid–liquid interfacial methods.[29,30]

The inherent Raman vibrational modes of the C_{60} monomer, particularly those localized at 1,463 cm^{-1}, 490 cm^{-1}, and 269 cm^{-1} (●), correspond to the Ag(2) "pentagonal pinch"

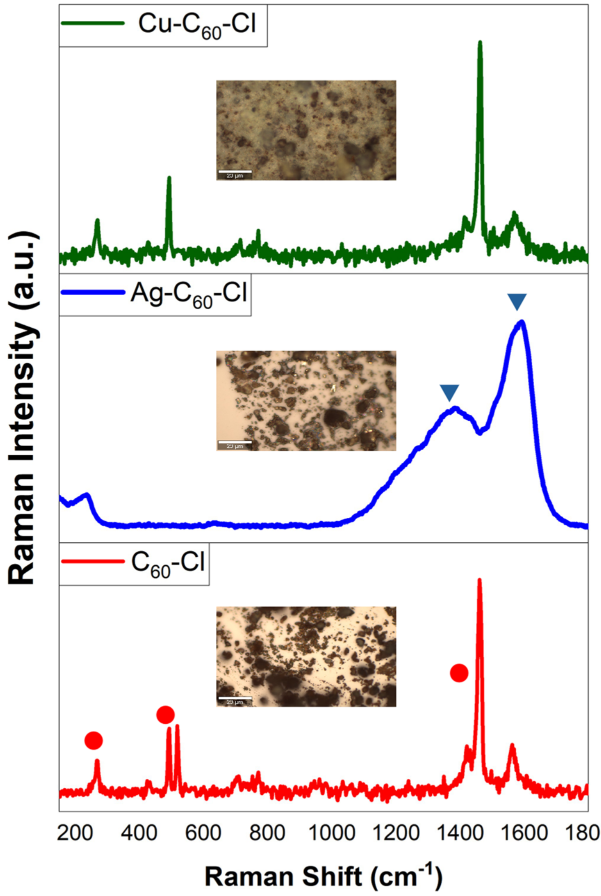

Fig. 2 Raman spectra and morphological images of C_{60}-Cl, Ag-C_{60}-Cl, and Cu-C_{60}-Cl fullerenes synthesized through the liquid–liquid interfacial method. The Raman spectra display the inherent vibrational modes of (red trace) C_{60}-Cl, (blue trace) Ag-C_{60}-Cl, and (green trace) Cu-C_{60}-Cl. Insets show the corresponding morphological images of the nanoparticles taken through a Raman microscope at 50× with a scale bar of 20 μm. All spectra were background-subtracted and normalized.

mode, Ag(1) "breathing," and Hg(1) squashing mode of C_{60} molecules, respectively. These modes disappeared in Ag-C_{60}-Cl nanoparticles due to the robust interaction between Ag-C_{60}-Cl, causing a severe reduction in fullerene symmetry. Consequently, two broadened and weakened peaks emerge, centered at 1,580 cm^{-1} and 1,361 cm^{-1} (▼), respectively. These results provide evidence of charge transfer between Ag^{+} and C_{60}-Cl, leading to charge redistribution and suppressing most Raman activity.[31] Other vibration bands, such as 1,560 cm^{-1} Hg(8) and 1,418 cm^{-1} Hg(7), associated with laser-induced C_{60}-Cl polymerization,[32] were entirely absent. This absence demonstrated that a cage-like Ag^{+} network isolates individual fullerene molecules, serving as a physical or structural impediment that prevents fullerene polymerization or linking together, and acts as a barrier to C_{60}-C_{60} cross-linking. In all spectra, the background was subtracted, and the spectra were normalized.

To further validate the experimental Raman results, computational Raman spectra were obtained, indicating that fullerenes can accommodate up to six silver or copper ions. To determine the spatial arrangement of these metal ions relative to the surface of fullerenes, experimental Raman spectra were compared with those generated computationally. Using Gaussian 16 software (Gaussian, Inc), Raman spectra for configurations with metal ions located internally (Fig. 3Ia) and externally (Fig. 3Ib) were simulated to ascertain their relaxed geometries and corresponding spectra. In alignment with previous computational studies of pristine fullerenes,[33] the B3LYP method[34] and the lanl2dz basis set,[35] augmented with Grimme's GD3 empirical dispersion correction,[36] were utilized.

The computational strategy was initially validated by simulating the Raman spectrum of chloro-fullerene (C_{60}-Cl) (Fig. 3II) and comparing it with both prior computational data[37] and experimental results (Fig. 2). Analysis of the spectra for Ag-C_{60}-Cl, both internally (Fig. 3III) and externally (Fig. 3IV), suggested an internal positioning of the metal ion, as inferred from the spectral peak alignment. Similarly, for Cu-C_{60}-Cl, the Raman spectra (Fig. 3V and VI) supported an internal location of the ion, corroborated by matching peaks with the experimental spectra (Fig. 2b and c). Nonetheless, data from Fig. 3IV and VI indicated external positioning for the metal ions in both copper and silver-coordinated fullerenes.

The electrostatic polarization of fullerenes, shown in Fig. 4, was also analyzed. Pristine fullerenes exhibit minimal electrostatic polarization due to the symmetric distribution of carbon atoms. In contrast, fullerenes modified with copper and silver atoms show increased polarization. This is attributed to the higher electronegativity which leads to repulsive interactions with the carbon framework.

X-ray photoelectron spectroscopy

The XPS survey results (Fig. 5) showed that C_{60}-Cl fullerenes demonstrate three dominant peaks at 199.8, 283.5, and 531.5 eV which correspond to Cl 2p, C 1s, and O 1s peaks, respectively, and confirmed the existence of sp2 and sp3 carbon along with the surface-bound oxygen groups. The C 1s spectrum showed a broad, asymmetric tail towards higher binding energy. Moreover, satellite features, located several eV from the main C 1s peak, were observed in the C_{60}-Cl fullerenes, indicating a high concentration of sp2-hybridized carbon. In Cl 2p spectrum, four distinct peaks were observed, corresponding to Cl $2p_{1/2}$ (at 199.4 eV), Cl $2p_{3/2}$(at 197.7 eV), carbon-Cl $2p_{1/2}$ (at 201.8 eV), and carbon-Cl $2p_{3/2}$ (at 200.4 eV).

In Fig. 6, the XPS survey revealed four dominant peaks at 283.5, 531.5, 368.2, and 200.0 eV, corresponding to C 1s, O 1s, Ag 3d, and Cl 2p peaks, respectively. The silver spectrum

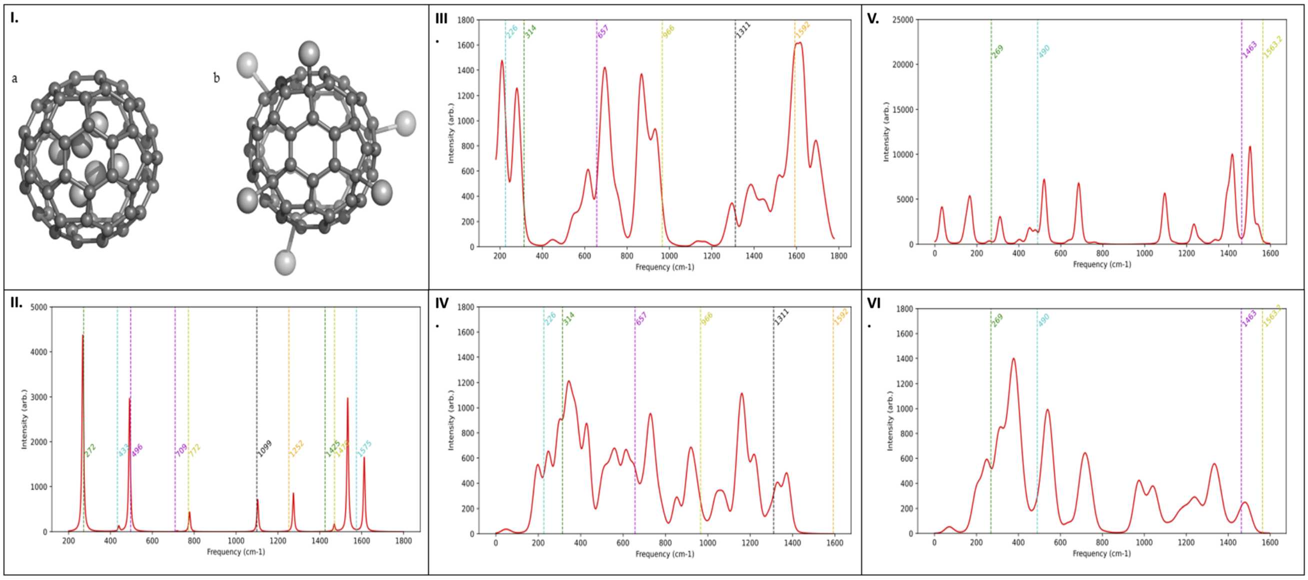

Fig. 3 (I) Graphical models illustration of relaxed geometry of six metal ions in relation to the fullerenes. (a) Configuration with six metal ions positioned inside the fullerene cage and (b) configuration with six metal ions positioned outside the fullerene cage. Theoretical Raman spectra for (II) C_{60}-Cl, (III) Ag ions outside the cage Ag-C_{60}-Cl, (IV) Ag ions inside the cage Ag-C_{60}-Cl, (V) Cu ions outside the cage Cu-C_{60}-Cl, and (VI) Cu ions inside the cage Cu-C_{60}-Cl. The spectral peak alignment is further corroborated by the matching peaks in the experimental spectra (Fig. 2).

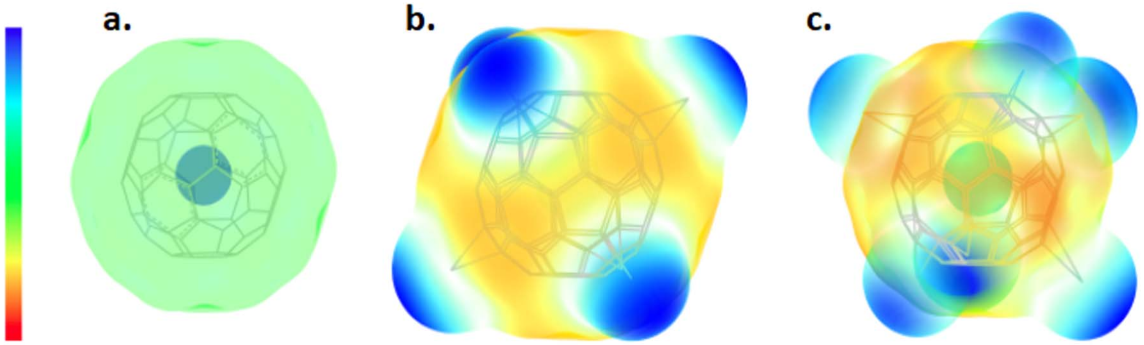

Fig. 4 Electrostatic potential mapped onto the total electron density of fullerenes. Isometric scale bar values are shown in blue (positive) and red (negative) for (a) pristine fullerene +/− 6.488 × 10^{-2} [eV], (b) fullerene modified with copper atoms exhibiting increased polarization and repulsive interactions with the carbon framework, with an isometric scale bar of +/− 4.52 × 10^{-2} [eV], and (c) fullerene modified with silver atoms also showing increased polarization and repulsive interactions with the carbon framework, with an isometric scale bar of +/− 3.594 × 10^{-2} [eV].

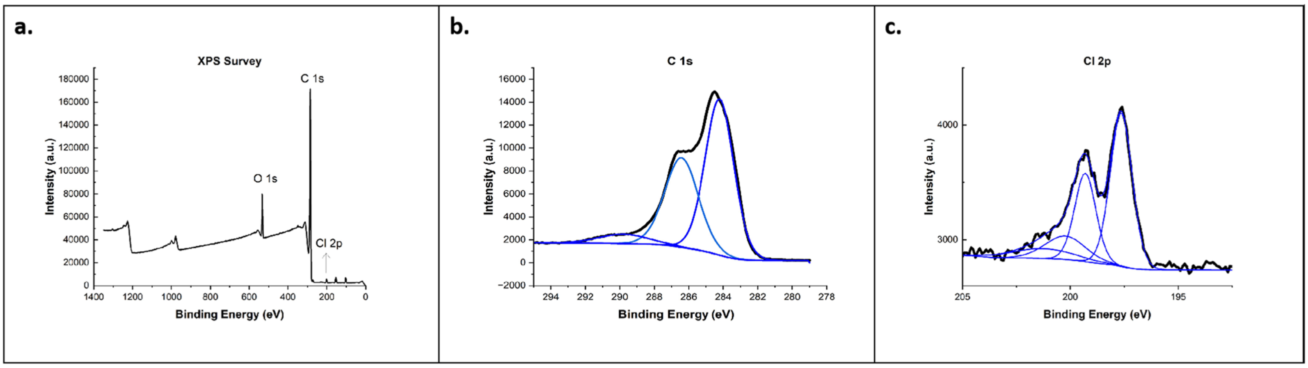

Fig. 5 (a) XPS survey spectra of C_{60}-Cl and high-resolution scans for (b) C 1s and (c) Cl 2p.

displayed well-separated spin-orbitals of Ag 3d at 367.76 and 373.77 eV, with no loss features. The C 1s spectrum of Ag-C_{60}-Cl showed a broad, asymmetric tail towards higher binding energy with lesser intensity and showed the absence of some functional groups (C═O and O–C═O), due to the binding of silver ions. In addition, no loss feature was shown in the C 1s spectrum of Ag-C_{60}-Cl, which might be due to the interaction of silver ions with the fullerenes. In Cl 2p spectrum, four peaks were shown, which are related to Cl $2p_{1/2}$ (at 199.2 eV), Cl $2p_{3/2}$ (at 198.4 eV), carbon-Cl $2p_{1/2}$ (at 201.4 eV), and carbon-Cl $2p_{3/2}$(at 200.4 eV).

In Fig. 7, the XPS survey demonstrated four dominant peaks at 283.5, 531.5, 934.79, and 200.0 eV correspond to C 1s, O 1s, Cu 2p, and Cl 2p peaks, respectively. The Cu 2p peak has significantly split spin–orbit components, with Cu(II)-carbonate showing a peak at 934.79 eV. Additionally, Cu(II) displayed a collection of observable satellite features at 944 eV. The Cu-C_{60}-Cl results for the C 1s and Cl 2p peaks showed similar behavior to Ag-C_{60}-Cl. In these XPS results, significant changes in the Cl 2p peaks between C_{60}-Cl, Ag-C_{60}-Cl, and Cu-C_{60}-Cl was shown. These changes are indicative of chlorine's role in enhancing the reactivity of the fullerenes. The Cl 2p peaks for Ag-C_{60}-Cl and Cu-C_{60}-Cl were more prominent, reflecting the stronger interaction between chlorine and the metal ions. This suggests that the coordination of chlorinated fullerenes with silver and copper plays a role in increasing the antibacterial effectiveness of the nanoparticles by promoting better interaction with bacterial cell membranes.

Scanning electron microscopy-energy dispersive X-ray

The SEM-EDS analysis was performed to understand the morphology and the elemental compositions in C_{60}-Cl, Ag-C_{60}-Cl, and Cu-C_{60}-Cl (Fig. 8). The SEM image (Fig. 8a) showed the globular shape of chlorine-functionalized C_{60}-Cl fullerene aggregates. The EDS results confirmed the presence of only C, O, Cl, and Si elements, where the presence of Si is due to the silicon substrate. Similarly, Ag-C_{60}-Cl fullerenes (Fig. 8b) showed a globular shape of chlorine-functionalized Ag-C_{60}-Cl fullerene aggregates. Interestingly, the EDS results confirmed the presence of only C, O, Cl, Ag elements, and Si substrate as well, which indicates the high purity of Ag-C_{60}-Cl fullerenes and the reliability of the present preparation method. Cu-C_{60}-Cl fullerenes (Fig. 8c) showed clusters of globular shapes of chlorine-functionalized Cu-C_{60}-Cl fullerene aggregates. In addition, EDS results confirmed the presence of only C, O, Cl, and Cu elements as well as the Si substrate. Taken together, the elemental mapping of the C_{60}-Cl, Ag-C_{60}-Cl, and Cu-C_{60}-Cl fullerenes confirmed the homogenous dispersion of the Ag and Cu.

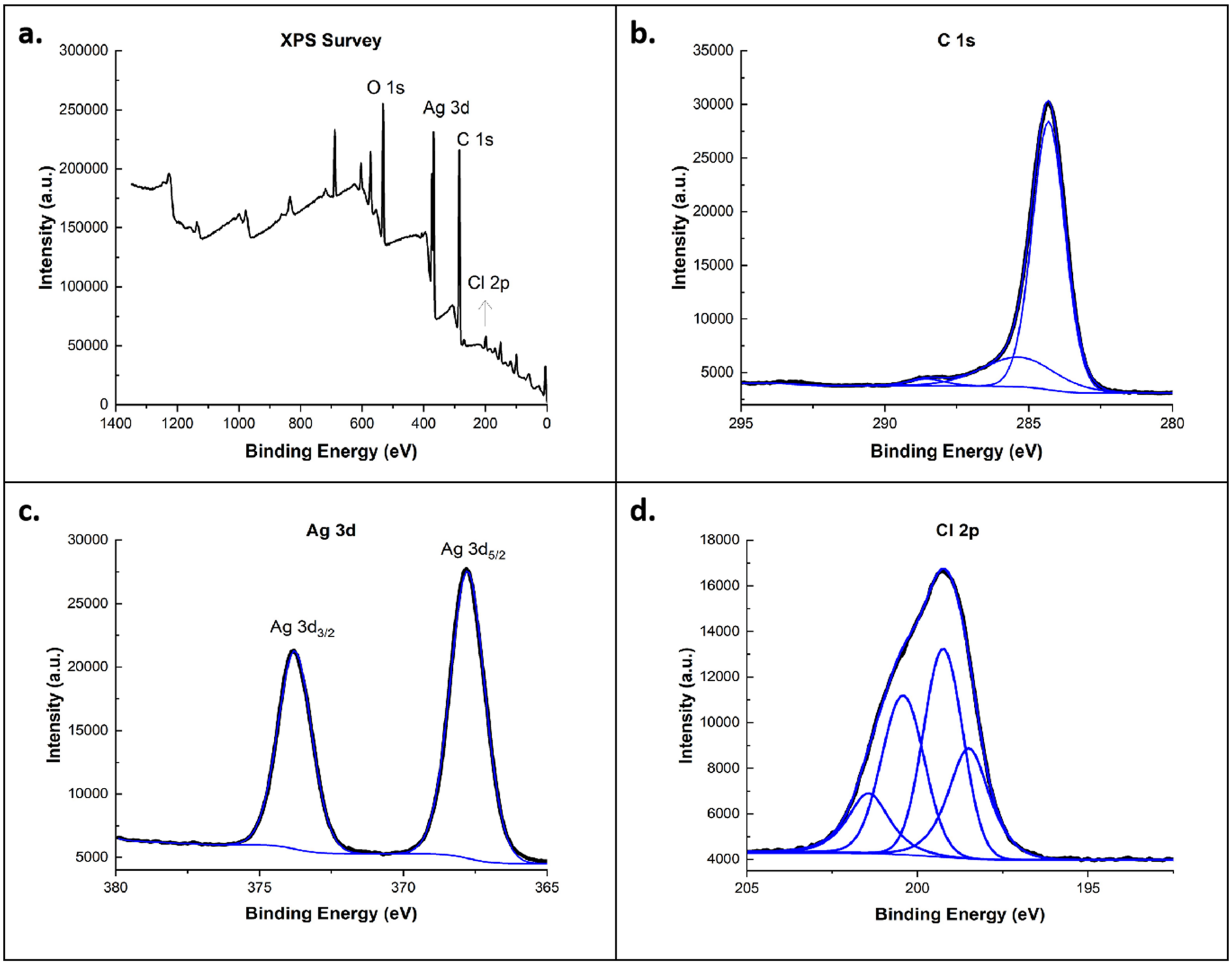

Fig. 6 (a) XPS survey spectra of Ag-C_{60}-Cl and high-resolution scans for (b) C 1s, (c) Ag 3d, and (d) Cl 2p.

Fourier-transform infrared spectroscopy

Fourier-transform infrared (FTIR) spectroscopy was performed to characterize the functionalization and coordination of metals with fullerenes. The spectra of pristine fullerene (C_{60}), chlorofullerene (C_{60}-Cl), and metal-coordinated fullerene complexes (Ag-C_{60}-Cl and Cu-C_{60}-Cl) have shown significant changes in vibrational modes (Fig. 9).

The FTIR spectra of C_{60} (in black) shows the characteristic absorption peaks associated with fullerene's vibrational modes. The primary infrared-active modes, attributed to the highly symmetric structure of C_{60}, appear at 526 cm^{-1} (radial breathing mode), 576 cm^{-1} (F_{1u} symmetry), 1182 cm^{-1}, and 1427 cm^{-1}. These peaks are indicative of the unique sp2 hybridization and spherical geometry of fullerene. These peaks corresponded to previously reported results in the literature.[38]

Upon chlorination, significant changes were observed in the FTIR spectrum (in red). A sharp new peak appears at 1214 cm^{-1}, which can be attributed to the C-Cl stretching vibration, confirming the successful functionalization of C_{60} with chlorine. The peak at 1729 cm^{-1}, present in both C_{60} and C_{60}-Cl spectra, likely corresponds to a carbonyl (C=O) group, suggesting possible oxidation of the fullerene nanoparticles. Notably, the peak at 1639 cm^{-1} observed in C_{60} disappeared in the C_{60}-Cl spectrum, indicating that functionalization alters the vibrational mode associated with this wavenumber. Furthermore, while the peak at 576 cm^{-1}, attributed to the radial breathing mode of C_{60}, is significantly reduced in C_{60}-Cl, the peak at 1427 cm^{-1} remains unchanged. This indicates that the core structure of C_{60} is largely preserved, but the vibrational modes associated with the fullerenes are modified by chlorination.

The coordination of silver to the chloro-fullerene (in blue) leads to noticeable shifts in the vibrational frequencies. A new peak appears around 1340 cm^{-1}, likely representing a modified vibrational mode associated with the interaction between the silver ion and the fullerene structure. Furthermore, the appearance of the peak at 1635 cm^{-1} suggests new vibrational interactions within the fullerene, possibly due to the influence of silver on the π-conjugated system of the fullerene, specifically the C=C bonds. These shifts and new peaks provide evidence that the coordination is likely occurring through the fullerene's double bonds, a common interaction observed in fullerene-metal systems, further supported by minor shifts in peaks

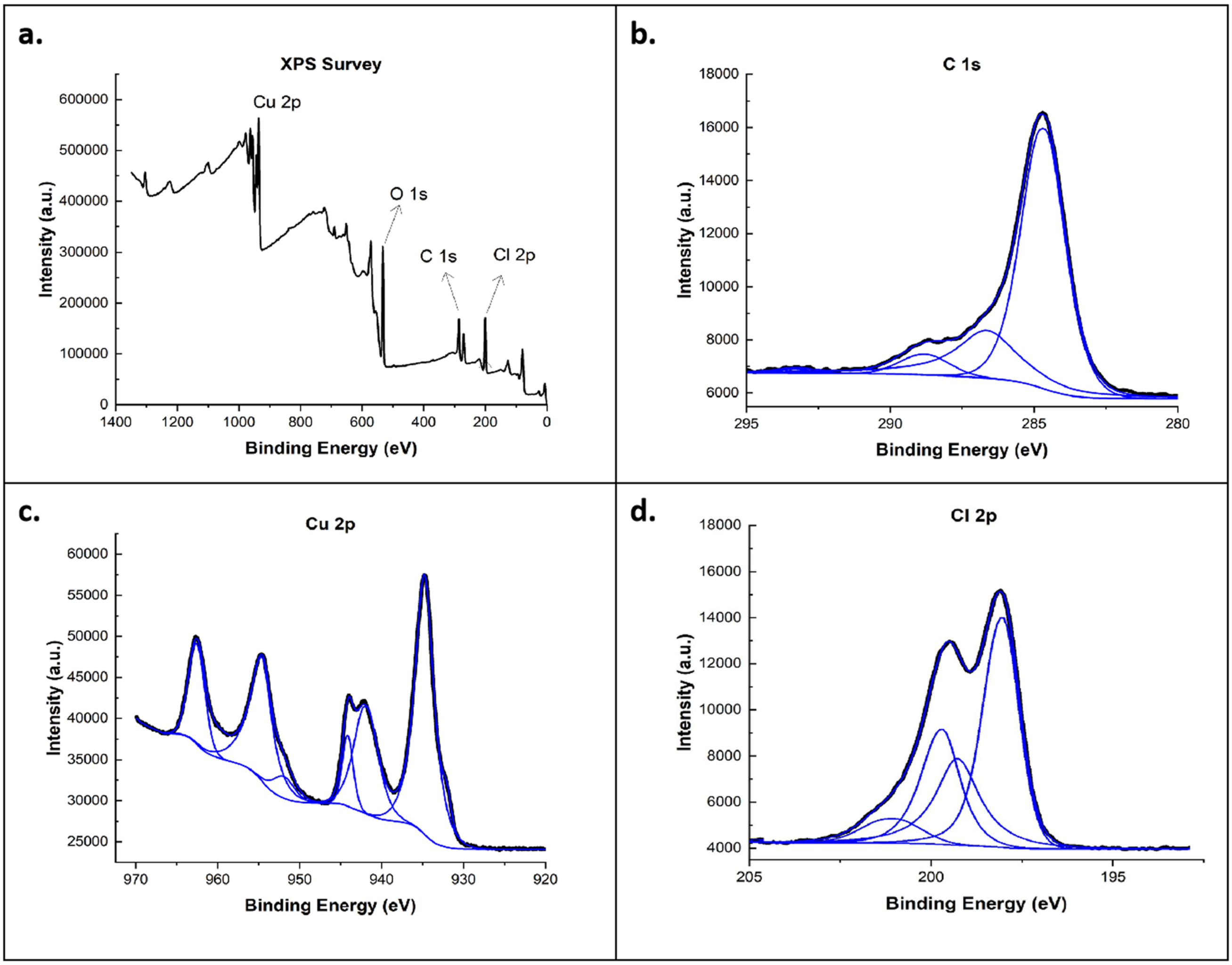

Fig. 7 (a) XPS survey spectra of Cu-C_{60}-Cl and high-resolution scans for (b) C 1s, (c) Cu 2p, and (d) Cl 2p.

associated with the fullerene core structure. In addition, the peak corresponding to the carbonyl stretch shifts slightly from 1729 cm^{-1} to 1733 cm^{-1}, which may suggest an interaction between the carbonyl group and the silver ion. This shift, alongside the increased sharpness of the peak, indicates potential stabilization of the C═O bond due to metal coordination.

Similarly, the Cu-C_{60}-Cl (in green) shows a shift in the carbonyl peak to 1735 cm^{-1}, but this peak appears sharper compared to the Ag-C_{60}-Cl spectrum. The sharpness indicates a stronger interaction between the copper ion and the fullerene carbonyl group, which could be due to the higher Lewis acidity of copper compared to silver. Additionally, there are small shifts in the C-Cl and fullerene-related peaks, signifying that copper has a more pronounced effect on the overall structure compared to silver.

High-resolution transmission electron microscopy

The morphological and structural properties of C_{60}, C_{60}-Cl, Ag-C_{60}-Cl, and Cu-C_{60}-Cl were investigated using Transmission Electron Microscopy (TEM) and Selected Area Electron Diffraction (SAED). The results provided insight into the aggregation behavior, structural integrity, and crystalline nature of the nanoparticles after functionalization and metal coordination.

TEM analysis of pristine C_{60} (Fig. 10a) shows clusters of aggregated fullerene particles. The aggregation, commonly observed in fullerene systems, results from van der Waals interactions between C_{60} molecules, leading to the formation of larger clusters. The corresponding SAED pattern (Fig. 10b) exhibits distinct diffraction rings, which confirm the crystalline nature of pristine C_{60}. This finding aligns with the high symmetry and molecular structure of C_{60}, further supported by FTIR analyses, which identified characteristic vibrational modes corresponding to the sp^2 hybridization of the fullerene framework.

Upon chlorination, the TEM image of C_{60}-Cl (Fig. 10c) shows an increase in particle aggregation compared to pristine C_{60}. This observation suggests that chlorination enhances the intermolecular interactions between fullerene molecules, leading to larger clusters. However, the SAED pattern (Fig. 10d) indicates reduced crystallinity in C_{60}-Cl compared to C_{60}, as evidenced by the less-defined diffraction rings. This reduction

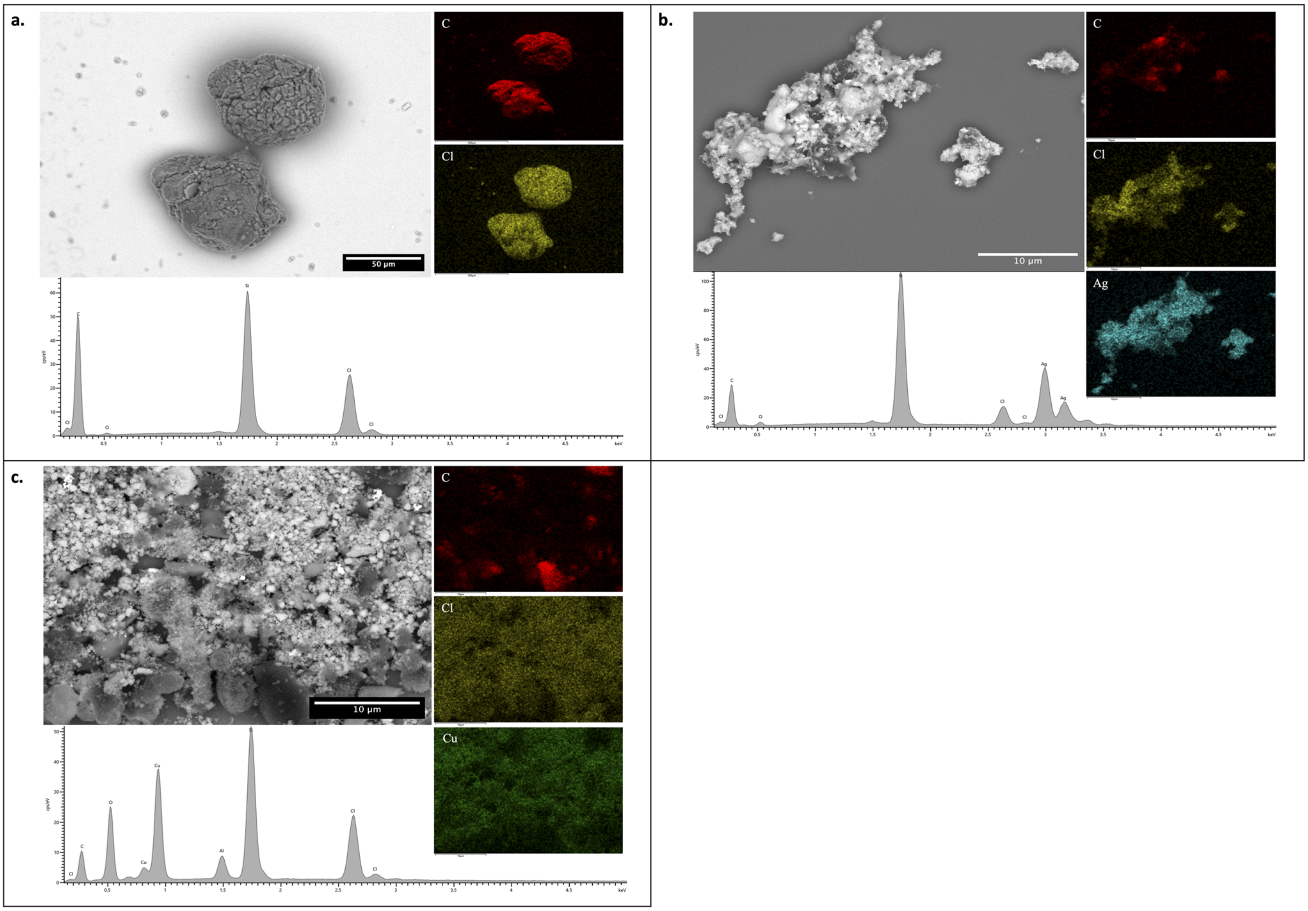

Fig. 8 SEM-EDS of C_{60}-Cl, Ag-C_{60}-Cl, and Cu-C_{60}-Cl fullerenes. SEM image and EDS results of (a) C_{60}-Cl, (b) Ag-C_{60}-Cl, and (c) Cu-C_{60}-Cl.

in crystallinity is likely due to the introduction of chlorine atoms, which disrupt the molecular symmetry of C_{60}. These changes are consistent with FTIR results, where the appearance of new peaks at 1214 cm^{-1} confirmed the C-Cl functionalization and a shift in the vibrational modes associated with the fullerene core structure.

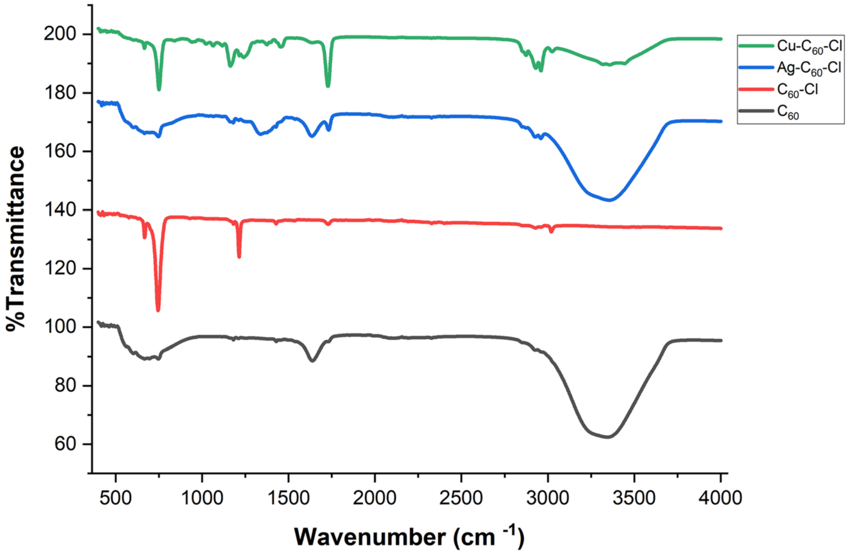

Fig. 9 FTIR spectra of C_{60}, C_{60}-Cl, Ag-C_{60}-Cl, and Cu-C_{60}-Cl fullerenes. The black FTIR spectrum represents pristine fullerenes, the red FTIR spectrum represents C_{60}-Cl, the blue represents Ag-C_{60}-Cl, and the green represents Cu-C_{60}-Cl.

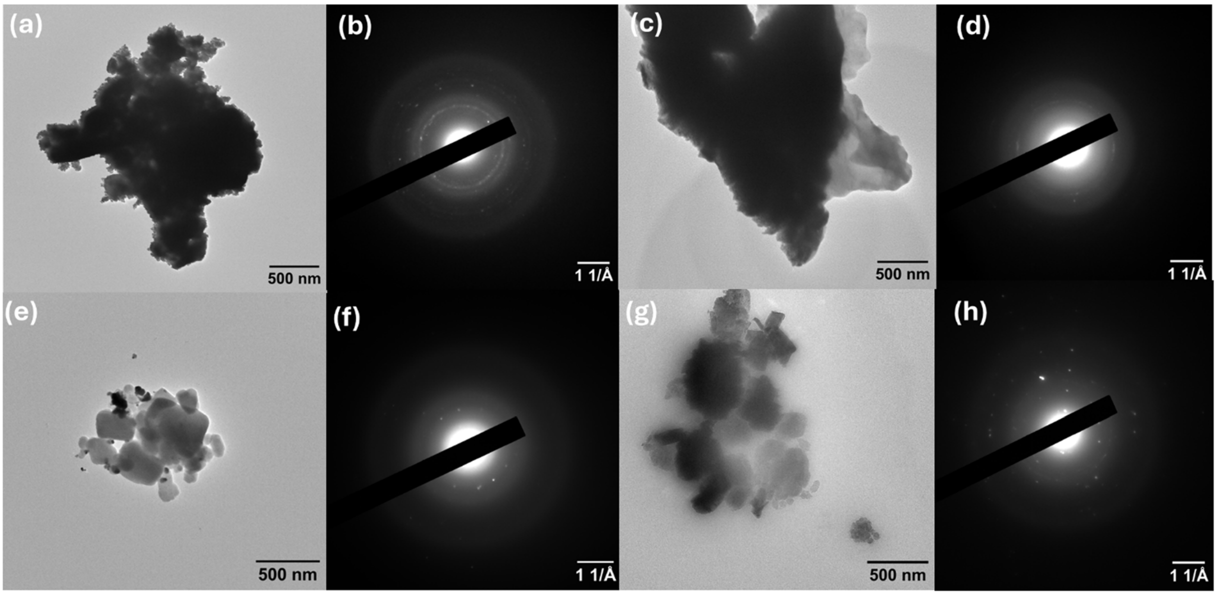

Fig. 10 (a) TEM image of C_{60} nanoparticles at 10k×; (b) corresponding SAED pattern of C_{60}; (c) TEM image of C_{60}-Cl at 10k×; (d) its corresponding SAED pattern; (e) TEM image of Ag-C_{60}-Cl at 10k×; (f) its corresponding SAED pattern; (g) TEM image of Cu-C_{60}-Cl at 10k×; (h) its corresponding SAED pattern.

For Ag-C_{60}-Cl (Fig. 10e), TEM reveals a more defined nanoparticle structure with less aggregation than C_{60}-Cl, suggesting that silver coordination affects the dispersion of fullerene nanoparticles. The SAED pattern (Fig. 10f) shows clear diffraction rings, indicating that Ag-C_{60}-Cl retains its crystallinity after silver coordination. The SAED analysis also reveals features corresponding to the silver's influence on the crystalline structure of the fullerene. These findings are consistent with FTIR results, which showed shifts in vibrational modes, including the carbonyl stretching at 1733 cm^{-1}, suggesting interaction between silver ions and the fullerene structure.

Finally, Cu-C_{60}-Cl (Fig. 10g) exhibits a distinct anisotropic morphology, with the nanoparticles displaying less aggregation and more uniform shapes compared to the Ag-C_{60}-Cl sample. The SAED pattern (Fig. 10h) reveals well-defined diffraction rings, indicating the crystalline structure of Cu-C_{60}-Cl. The SAED results correlate with the structural rearrangement observed in the FTIR spectra, where a shift in the carbonyl stretching frequency to 1735 cm^{-1} suggests stronger coordination between the copper ions and fullerene.

Disc diffusion assay

The antibacterial activity of C_{60}-Cl, Ag-C_{60}-Cl, and Cu-C_{60}-Cl was evaluated against two bacterial strains, the Gram-negative *E. coli* and Gram-positive MRSA. Compared to the C_{60}-Cl control, which showed no zones, the inhibition zones produced by Ag-C_{60}-Cl and Cu-C_{60}-Cl were 15 mm and 7 mm, respectively. Similarly, Ag-C_{60}-Cl produced the highest zone of inhibition (14 mm) against MRSA compared to Cu-C_{60}-Cl (10 mm) and C_{60}-Cl which produced no zones (see ESI†). It was shown that Ag-based fullerenes were more active than pristine fullerenes alone and Cu-based fullerenes.

The differences in the antimicrobial properties might have been attributed to the synergism of Ag^+ ions and fullerenes. The coordination of Ag in fullerenes produced enhanced antimicrobial potential as compared to control. Because, in integrated form, the Ag ions stabilized with the carbon cage confer increased concentration at the desired site and result in enhanced antimicrobial activities.[39]

Minimum inhibition concentration

The microdilution assay performed to determine the MIC of all types of nanoparticles showed that C_{60}-Cl fullerenes were active at higher concentrations compared to fullerenes incorporated with silver and copper. In general, Ag-C_{60}-Cl fullerenes showed the highest activity at lower concentrations compared to C_{60}-Cl and Cu-C_{60}-Cl fullerenes.

When applied against *E. coli*, Ag-C_{60}-Cl resulted in inhibition of growth at the lower MICs (3.906 μg mL^{-1}), while Cu-C_{60}-Cl inhibited growth at 125 μg mL^{-1} compared to control C_{60}-Cl (>500 μg mL^{-1}). Similarly, consistent with our previous findings in the disk diffusion assay, the lowest MICs were observed with Ag-based fullerenes against both *E. coli* and MRSA. Ag-C_{60}-Cl inhibited the growth of MRSA at 3.906 μg mL^{-1} compared to Cu-C_{60}-Cl (125 μg mL^{-1}) and C_{60}-Cl (>500 μg mL^{-1}). The MICs of each fullerene evaluated are shown in Tables 1 and 2.

Efflux pump inhibition assay

The cartwheel assay was performed to assess the ability of bacteria to expel EtBr. Ethidium bromide is a substrate for efflux pumps and bacteria having an active efflux pump expel it out of the cell once taken in from the media along with nutrients.[40] Once faced with any active efflux pump inhibitor, EtBr remains inside of the cell and forms a reddish pattern along the lines of

Table 1 Minimum inhibitory concentration (MIC) against *E. coli*, turbidity for different concentrations of nanoparticles after 24 h[a]

Dilution of the nanoparticles	500 μg mL^{-1}	250 μg mL^{-1}	125 μg mL^{-1}	62.5 μg mL^{-1}	31.25 μg mL^{-1}	15.625 μg mL^{-1}	7.8125 μg mL^{-1}	3.906 μg mL^{-1}	1.953 μg mL^{-1}	0.9765 μg mL^{-1}
$AgNO_3$	−	−	−	−	−	−	−	+	+	+
	−	−	−	−	−	−	−	+	+	+
C_{60}-Cl	+	+	+	+	+	+	+	+	+	+
	+	+	+	+	+	+	+	+	+	+
Ag-C_{60}-Cl	−	−	−	−	−	−	−	−	+	+
	−	−	−	−	−	−	−	−	+	+
Cu-C_{60}-Cl	−	−	−	+	+	+	+	+	+	+
	−	−	−	+	+	+	+	+	+	+

[a] Positive (+): turbidity indicating growth; negative (−): no turbidity indicating absence of growth.

Table 2 Minimum inhibitory concentration (MIC) against MRSA, turbidity for different concentrations of nanoparticles after 24 h[a]

Dilution of the nanoparticles	500 μg mL^{-1}	250 μg mL^{-1}	125 μg mL^{-1}	62.5 μg mL^{-1}	31.25 μg mL^{-1}	15.625 μg mL^{-1}	7.8125 μg mL^{-1}	3.906 μg mL^{-1}	1.953 μg mL^{-1}	0.9765 μg mL^{-1}
$AgNO_3$	−	−	−	−	−	−	−	+	+	+
	−	−	−	−	−	−	−	+	+	+
C_{60}-Cl	+	+	+	+	+	+	+	+	+	+
	+	+	+	+	+	+	+	+	+	+
Ag-C_{60}-Cl	−	−	−	−	−	−	−	−	+	+
	−	−	−	−	−	−	−	−	+	+
Cu-C_{60}-Cl	−	−	−	+	+	+	+	+	+	+
	−	−	−	+	+	+	+	+	+	+

[a] Positive (+): turbidity indicating growth; negative (−): no turbidity indicating absence of growth.

bacterial growth in the cartwheel pattern. In *E. coli*, efflux pumps play a major role in antibiotic resistance by actively expelling a wide range of antibiotics, thereby decreasing their intracellular concentrations and effectiveness. This system is particularly notable for its contribution to resistance against multiple antibiotics.

On the other hand, MRSA, also possesses multiple efflux pumps, which contribute to its resistance profile, but other mechanisms like β-lactamase production and alterations in penicillin-binding proteins play substantial roles.[41] Comparatively, the activity of efflux pumps in *E. coli* is generally considered to be more significant in its contribution to

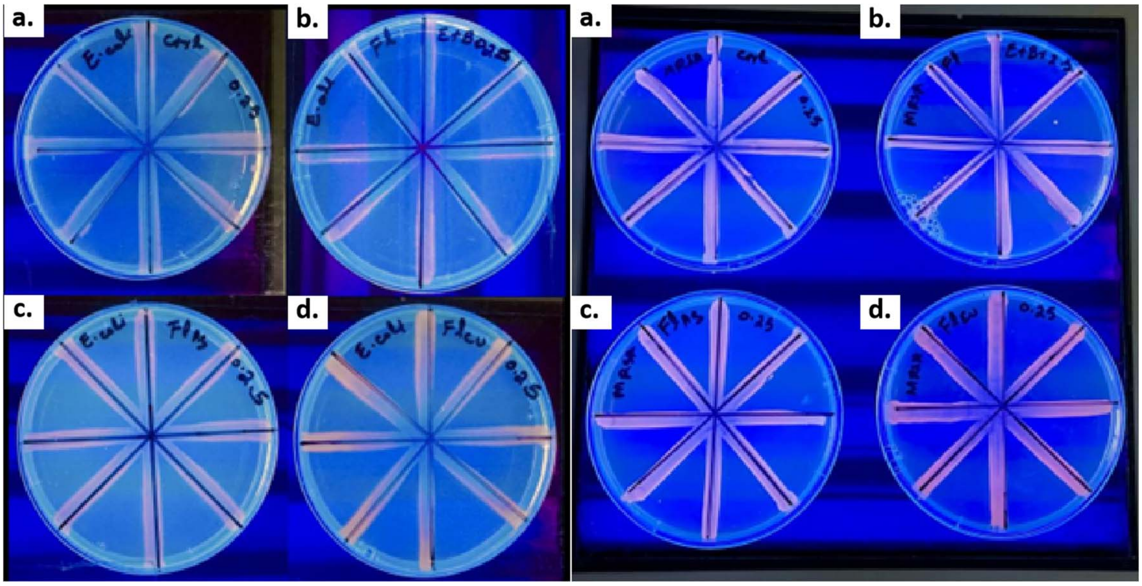

Fig. 11 EtBr cartwheel assay assessing efflux pump inhibition in *E. coli* and MRSA. Evaluation of (a) control (without nanoparticles), (b) C_{60}-Cl fullerenes, (c) Ag-C_{60}-Cl fullerenes, and (d) Cu-C_{60}-Cl fullerenes in *E. coli* and MRSA.

multidrug resistance due to the broad substrate range and high efficiency pumps, which can handle a wide array of antibiotics and toxic substances. The results indicated that the efflux pump was very active in *E. coli*, whereas they were slightly less active in MRSA. However, when applied with 0.5× MIC of C_{60}-Cl, Ag-C_{60}-Cl, and Cu-C_{60}-Cl, it was clearly observed, as compared to the control (devoid of nanoparticles), that the cells along the lines have more entrapped EtBr.

In contrast to the antibacterial activity, however, Cu-C_{60}-Cl seems to be more active in efflux pump inhibition than Ag-C_{60}-Cl and C_{60}-Cl. Furthermore, the efflux pump of MRSA was less active, and thus, EtBr was trapped inside, even in the absence of added fullerenes. However, as shown in Fig. 11, Cu-C_{60}-Cl appeared in bright red, indicating the presence of higher concentrations of EtBr inside of the cells. This difference in efficiency can be attributed to the structural and functional characteristics of the respective efflux systems, making *E. coli*'s efflux systems more efficient at expelling various substances compared to those in MRSA. Together, these results indicated that Cu-C_{60}-Cl fullerenes were more potent in the inhibition of the efflux pump and copper seems to be actively inhibiting, as previously shown by Christena *et al.* (2015), wherein it was reported that copper nanoparticles potently inhibited the efflux pump in *S. aureus*.[28]

Reactive oxygen species quantification

Bacteria produce ROS when exposed to stress such as that coming from antimicrobial compounds. It has previously been reported that intracellular oxide radicals are formed in bacteria when treated with metallic nanoparticles. In this study, we observed that fullerenes and fullerene derivatives were able to induce ROS formation in both *E. coli* and MRSA (Fig. 12). The ROS production was expressed and recorded in terms of fluorescence intensity. The highest amount of ROS, as evident by high fluorescence intensity, was generated in MRSA treated with Ag-C_{60}-Cl at 0.5× of MIC. The fluorescence intensity varied among the different bacterial strains. *E. coli*, when treated with all types of fullerenes, revealed generally lower ROS production than the levels observed in MRSA. It has been studied that various bacteria capable of tolerating and neutralizing ROS will produce less fluorescence intensity. Of note, the highest amount of ROS produced in *E. coli* was a result of treatment with C_{60}-Cl at 0.5× MIC.

The silver coordinated fullerenes used in the ROS experiment had a concentration of 1.953 μg mL^{-1} (0.5 MIC) compared to 250 μg mL^{-1} of C_{60}-Cl control (0.5 MIC). Thus, the coordination of silver on the fullerenes enhanced the activity of the nanoparticles to generate similar ROS at a 128-fold concentration difference. These results also showed that Cu-C_{60}-Cl was unable to generate higher levels of ROS against both *E. coli* and MRSA. This may be attributed to copper's known role as a scavenger of ROS, suggesting that any ROS induced by C_{60}-Cl could have been quenched by the associated copper. Thus, it can be concluded that the Ag-C_{60}-Cl produced antibacterial activity through increased ROS production. ROS production was measured in *E. coli* and MRSA treated with C_{60}-Cl, Ag-C_{60}-Cl, and Cu-C_{60}-Cl nanoparticles at varying concentrations (0.031 to 0.5 MIC). Statistical analysis using a two-tailed *t*-test were performed to assess the significance of differences between the nanoparticle treatments.

For *E. coli*, C_{60}-Cl *vs.* Ag-C_{60}-Cl resulted in a significant increase in ROS production ($P < 0.05$) in the Ag-C_{60}-Cl-treated group compared to the C_{60}-Cl-treated group ($P < 0.05$). This indicates that Ag functionalization significantly enhanced ROS generation compared to non-functionalized C_{60}-Cl

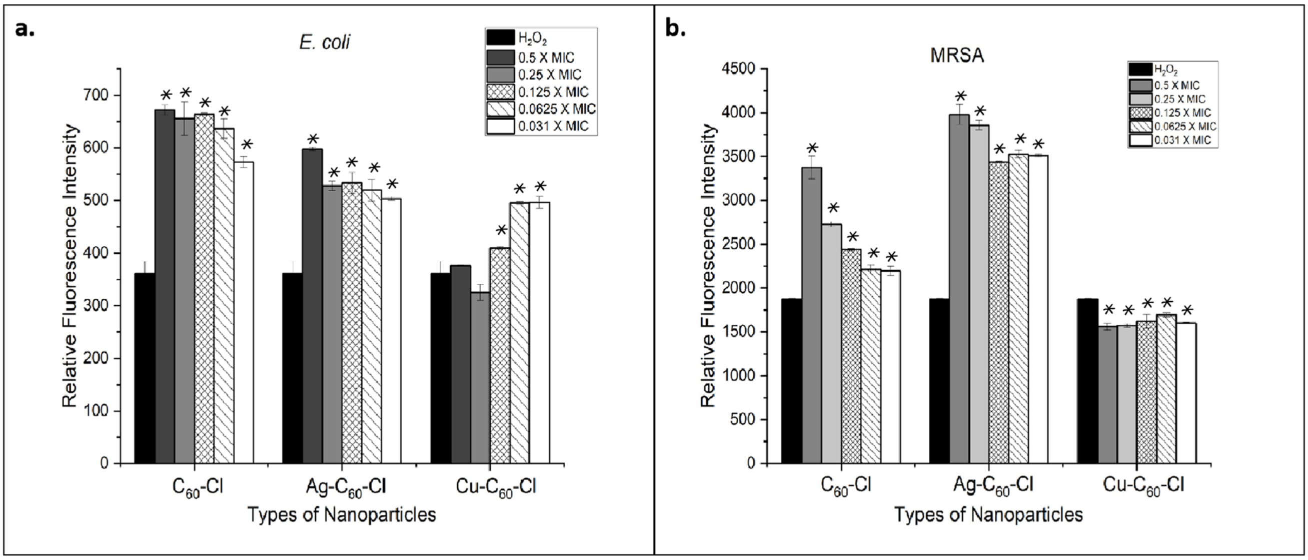

Fig. 12 Relative fluorescence intensity indicating ROS production in *E. coli* and MRSA treated with C_{60}-Cl, Ag-C_{60}-Cl, and Cu-C_{60}-Cl fullerenes. (a) *E. coli* and (b) MRSA were treated with increasing concentrations of C_{60}-Cl, Ag-C_{60}-Cl, and Cu-C_{60}-Cl fullerenes from 0.031 MIC to 0.5× MIC, or H_2O_2 alone (control). Data is represented by three independent assays (+/−SD). Statistical significance was determined using a *T*-test, comparing the MIC-treated samples to the H_2O_2 control, a potent inducer of ROS. Significance is denoted as $p > 0.05$ (*).

nanoparticles. For C_{60}-Cl *vs.* Cu-C_{60}-Cl, Cu-C_{60}-Cl-treated *E. coli* also exhibited a statistically significant increase in ROS production compared to the C_{60}-Cl group ($P < 0.05$). This also suggests that Cu functionalization also leads to higher ROS production. Lastly, in a comparison between Ag-C_{60}-Cl *vs.* Cu-C_{60}-Cl, Ag-C_{60}-Cl induced significantly higher ROS production compared to Cu-C_{60}-Cl ($P < 0.05$), indicating that silver functionalization has a stronger effect on ROS generation than copper.

Similar behavior was shown in MRSA; where in C_{60}-Cl *vs.* Ag-C_{60}-Cl, Ag-C_{60}-Cl nanoparticles produced significantly higher levels of ROS compared to C_{60}-Cl ($P < 0.05$), similar to the trend observed in *E. coli*. Additionally, C_{60}-Cl *vs.* Cu-C_{60}-Cl showed that Cu-C_{60}-Cl treatment led to significantly higher ROS production compared to C_{60}-Cl ($P < 0.05$), indicating that copper also enhances ROS production in MRSA. Finally, in the comparison between Ag-C_{60}-Cl *vs.* Cu-C_{60}-Cl, the ROS production in the Ag-C_{60}-Cl-treated MRSA group was significantly higher than in the Cu-C_{60}-Cl-treated group ($P < 0.05$), suggesting that Ag functionalization has a more pronounced effect on ROS generation than Cu functionalization.

Catalase assay

Catalase, an important antioxidant enzyme, can be triggered in response to oxidative damage to bacterial cells. For instance, ROS induced by nanoparticles could induce higher catalase production in bacteria, which acts as its antioxidant defense system.[42] The activity of catalase in both *E. coli* and MRSA was assessed in response to oxidative stress induced by fullerenes and fullerene derivatives (Fig. 13). Ag-C_{60}-Cl produced the highest change in fluorescence which indicated the highest catalase activity induced in both *E. coli* and MRSA. This was followed by C_{60}-Cl, while Cu-C_{60}-Cl induced the lowest catalase activity, which corresponds to the lowest levels of ROS generated by these three fullerenes.

It can be inferred that the production of ROS and catalase activity involves a delicate balance between the generated radicals and the enzyme's activity. Whereas, generally, the higher the ROS level, the higher the catalase activity against them. However, these results indicated that higher catalase activity in *E. coli* was accompanied by lower ROS levels in these cells (Fig. 12). This could imply that catalase effectively neutralized the free radicals within the cells, which previous reports have shown that catalase typically neutralizes oxides, peroxide, and superoxide radicals, thus protecting cells from their damage.[43]

Catalase activity was measured in *E. coli* and MRSA treated with C_{60}-Cl, Ag-C_{60}-Cl, and Cu-C_{60}-Cl nanoparticles. Statistical analysis using a two-tailed *t*-test was performed to assess the

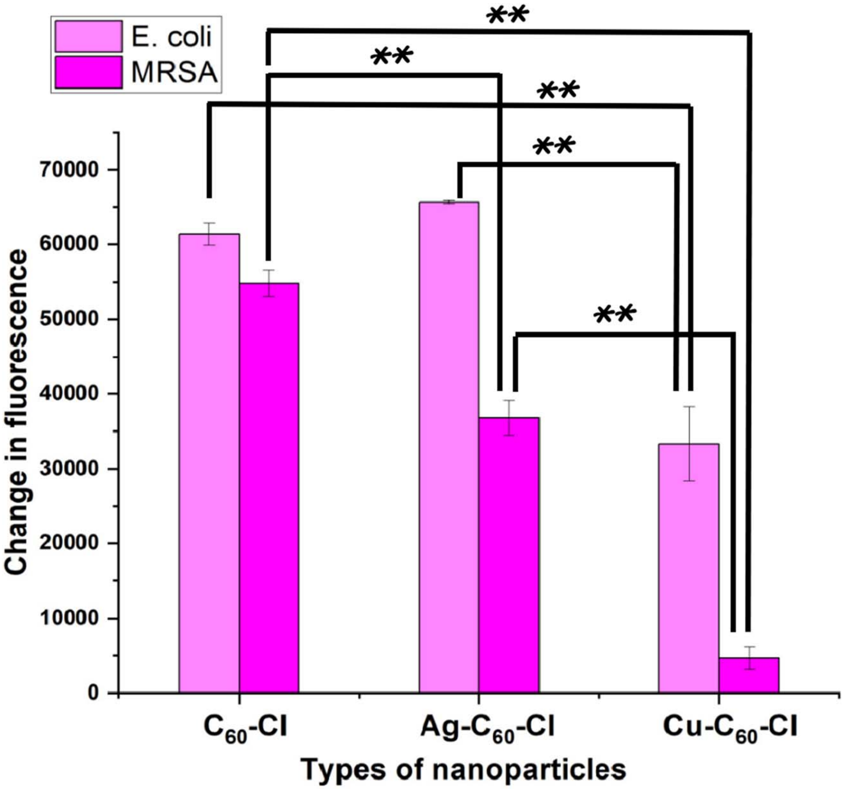

Fig. 13 Change in fluorescence indicating catalase activity in *E. coli* and MRSA treated with C_{60}-Cl, Ag-C_{60}-Cl, and Cu-C_{60}-Cl nanoparticles. *E. coli* and MRSA were treated with C_{60}-Cl, Ag-C_{60}-Cl, and Cu-C_{60}-Cl fullerenes with concentrations ranging from 7.8–500 µg mL^{-1}, along with appropriate controls. Data is represented by three independent assays (+/−SD). Statistical significance was determined using a *T*-test. Significance is denoted as follows: $p > 0.05$ (*) and $p \leq 0.005$ (**). Significant differences between nanoparticle treatments are indicated by brackets above the bars.

significance of differences between the nanoparticle treatments.

For *E. coli*, C_{60}-Cl *vs.* Ag-C_{60}-Cl resulted in a significant increase in catalase activity in the Ag-C_{60}-Cl-treated group compared to the C_{60}-treated group ($P < 0.05$). This indicates that silver functionalization significantly enhances catalase activity compared to non-functionalized C_{60}-Cl nanoparticles. For C_{60}-Cl *vs.* Cu-C_{60}-Cl, the Cu-C_{60}-Cl-treated *E. coli* exhibited a statistically significant decrease in catalase activity compared to the C_{60} group ($P < 0.005$), suggesting that copper functionalization leads to lower catalase activity. Lastly, in a comparison between Ag-C_{60}-Cl *vs.* Cu-C_{60}-Cl, Ag-C_{60}-Cl induced significantly higher catalase activity compared to Cu-C_{60}-Cl ($P < 0.005$), indicating that silver functionalization has a stronger effect on catalase activity than copper in *E. coli*.

A similar behavior was observed in MRSA; where in C_{60}-Cl *vs.* Ag-C_{60}-Cl, Ag-C_{60}-Cl nanoparticles produced significantly higher levels of catalase activity compared to C_{60} ($P < 0.005$), similar to the trend observed in *E. coli*. Additionally, C_{60}-Cl *vs.* Cu-C_{60}-Cl showed that Cu-C_{60}-Cl treatment led to significantly lower catalase activity compared to C_{60}-Cl ($P < 0.005$), indicating that copper reduces catalase activity in MRSA as well. Finally, in the comparison between Ag-C_{60}-Cl *vs.* Cu-C_{60}-Cl, the catalase activity in the Ag-C_{60}-Cl-treated MRSA group was significantly higher than in the Cu-C_{60}-Cl-treated group ($P < 0.005$), suggesting that Ag functionalization has a more pronounced effect on catalase activity than Cu functionalization in MRSA.

Dynamic light scattering and bacteria interactions

The particle size, distribution, and zeta potential of the nanoparticles were measured using a Malvern ZEN3600 Zetasizer to evaluate the colloidal stability and surface charge characteristics of the silver- and copper-coordinated chloro-fullerenes (Ag-C_{60}-Cl and Cu-C_{60}-Cl), as well as the control sample (C_{60}-Cl). Zeta potential measurements were conducted in replicates, as shown in the ESI.†

The Ag-C_{60}-Cl nanoparticles exhibited a Z-average size of 827.31 nm, and a zeta potential of −47.48 mV. The strongly negative surface charge indicates excellent colloidal stability due to electrostatic repulsion between particles, effectively preventing aggregation. This high stability allows Ag-C_{60}-Cl nanoparticles to remain well-dispersed in solution, which likely increases their interaction with bacterial cells, thereby enhancing their antibacterial activity. Additionally, the wall zeta potential of −59.09 mV confirms the stability of Ag-C_{60}-Cl in suspension.

For Cu-C_{60}-Cl, a larger average size of 1044.48 nm where the zeta potential was determined to be +25.4 mV, suggesting moderate colloidal stability. While this value is slightly lower than the threshold for ideal long-term suspension stability, the positive surface charge is of particular interest due to its potential for strong electrostatic interaction with the negatively charged bacterial cell membranes which was proven in the SEM image (Fig. 14) for the interaction between the bacteria and Cu-C_{60}-Cl nanoparticles. This enhanced interaction could facilitate more effective disruption of bacterial cells and contribute to the previously observed antibacterial properties of the Cu-C_{60}-Cl nanoparticles. The wall zeta potential of Cu-C_{60}-Cl was measured at −8.67 mV, reflecting a lower surface charge and suggesting that these particles may have a different interaction profile compared to Ag-C_{60}-Cl.

In comparison, the control sample C_{60}-Cl exhibited a Z-average size of 774.945 nm and a zeta potential of −58.38 mV, indicating superior colloidal stability, even higher than Ag-C_{60}-Cl. This result suggests that C_{60}-Cl nanoparticles remain highly stable in suspension, which is beneficial for prolonged interactions with bacterial cells. The wall zeta potential of −81.21 mV further highlights the enhanced stability of the C_{60}-Cl nanoparticles.

To further explain the interaction between the nanoparticles and the bacteria cells, SEM images for the nanoparticles–bacteria interaction were obtained as shown in Fig. 14. The images clearly depict the differences in bacterial morphology before and after nanoparticle treatment. In the control group, both *E. coli* and MRSA cells retain their intact, smooth morphology. After treatment with C_{60}-Cl, Ag-C_{60}-Cl, and Cu-C_{60}-Cl bacterial cells showed no significant membrane

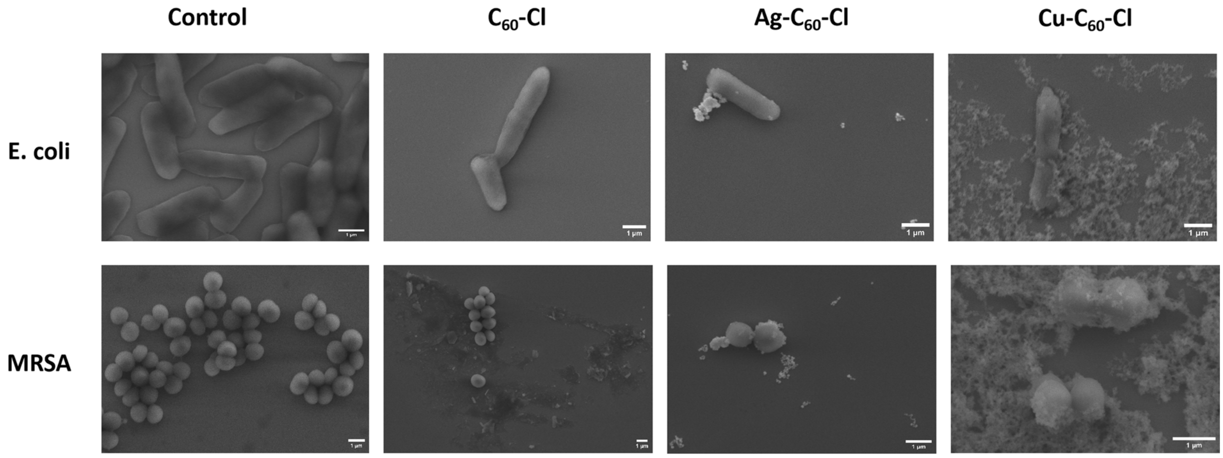

Fig. 14 SEM images for *E. coli* and MRSA before and after the treatment with C_{60}-Cl, Ag-C_{60}-Cl, and Cu-C_{60}-Cl nanoparticles.

deformation, indicating no external effect upon the interaction. In C_{60}-Cl no interaction with nanoparticles was shown indicating less selectivity to these nanoparticles. In contrast, the silver-coordination has shown enhanced interaction and furthermore for the copper-coordination. This comprehensive analysis of zeta potential, particle size, and SEM images demonstrates that Ag-C_{60}-Cl and Cu-C_{60}-Cl exhibited stronger antibacterial properties compared to C_{60}-Cl, with metal coordination amplifying the nanoparticles' interactions with bacterial membranes and contributing to higher antimicrobial efficacy.

Discussion

This study sought to provide insight into the antimicrobial properties, mechanisms of action, antioxidant defense system, and potential applications of fullerene metal conjugates in combating healthcare specific bacterial infections. The research describes a novel, rapid one-step synthesis method for producing Ag-C_{60}-Cl and Cu-C_{60}-Cl and evaluates their antibacterial efficacy against Gram-negative bacteria, *E. coli*, and a clinically relevant AMR Gram-positive bacteria, MRSA, revealing MICs of 3.9 $\mu g\ mL^{-1}$ and 125 $\mu g\ mL^{-1}$, respectively.

Pan *et al.* previously described the antibacterial activity of silver-modified fullerene towards *S. aureus*.[44] Herein, this research aligns with prior work and broadens applicability by leveraging Ag-C_{60}-Cl. The enhanced properties of Ag-C_{60}-Cl advance earlier work in this field by demonstrating biocidal properties against different bacterial strains, including resistant strains like MRSA and *E. coli*. These results emphasize the broad-spectrum utility and effectiveness of these novel nanoparticles in combating a wide range of bacterial pathogens. The future potential of these nanoparticles in clinical settings, especially in healthcare environments facing the unabated rise of AMR ‘superbugs’, could significantly enhance treatment approaches and strategies.

The results demonstrated that the metallic integration with fullerene significantly boosted inherent antimicrobial properties. The stability and increased surface reactivity of the Ag-C_{60}-Cl and Cu-C_{60}-Cl fullerene conjugates allowed for more effective interaction with bacterial membranes, leading to enhanced bacterial inhibition. The silver-coordinated nanoparticles exhibited potent activity against both Gram-negative and Gram-positive bacteria, while the copper-coordinated nanoparticles demonstrated notable antibacterial properties. This difference in activity could be attributed to the distinct interactions between the metal ions and the fullerene structures.

Reactive oxygen species (ROS) quantification, catalase assays, and efflux pump inhibition studies further elucidated the antibacterial mechanisms of the nanoparticles. The results revealed that Ag-C_{60}-Cl fullerenes induced higher ROS production, correlating with their enhanced antibacterial activity. In contrast, Cu-C_{60}-Cl fullerenes exhibited lower ROS levels, likely due to copper's known ROS-scavenging properties. This indicates that the antibacterial effect of Ag-C_{60}-Cl is primarily mediated through ROS generation, whereas the mechanism for Cu-C_{60}-Cl may involve other pathways, potentially through efflux pump inhibition. In general *E. coli* tends to be more resistant to antimicrobial agents compared to Gram-positive bacteria like *S. aureus*, due to the presence of a protective outer membrane. However, the findings in this research align with recent studies that suggest fullerene derivatives can exhibit broad-spectrum antimicrobial activity that impact both Gram-positive and Gram-negative bacteria similarly. For instance, the study by Bolshakova *et al.* (2023) demonstrated that fullerene derivatives on a nanodiamond platform show significant antimicrobial properties against a variety of bacteria, including *E. coli* and *S. aureus*.[45] This broad-spectrum activity is

Table 3 A comparison of this work with relevant studies from the literature

Nanomaterial	Bacterial strain	Minimum inhibitory concentration (MIC)	Antibacterial activity (zone of inhibition)	Relevant study/reference
C_{60} fullerenes	*Escherichia coli*	>500 $\mu g\ mL^{-1}$	No zone of inhibition	This work
Ag-C_{60}-Cl nanoparticles	*Escherichia coli*	3.9 $\mu g\ mL^{-1}$	15 mm	
	MRSA	3.9 $\mu g\ mL^{-1}$	14 mm	
Cu-C_{60}-Cl nanoparticles	*Escherichia coli*	125 $\mu g\ mL^{-1}$	7 mm	
	MRSA	125 $\mu g\ mL^{-1}$	10 mm	
THF/nC_{60}	*Bacillus subtilis*	0.08–0.10 $mg\ L^{-1}$	—	Lyon *et al.*[53]
THF/nC_{60} small		0.008–0.010 $mg\ L^{-1}$		
THF/nC_{60} large		0.6–0.8 $mg\ L^{-1}$		
Son/nC_{60}		0.4–0.6 $mg\ L^{-1}$		
Son/nC_{60} small		0.15–0.20 $mg\ L^{-1}$		
Son/nC_{60} large		0.6–0.8 $mg\ L^{-1}$		
Aq/nC_{60}		0.4–0.6 $mg\ L^{-1}$		
Aq/nC_{60} small		0.1–0.23 $mg\ L^{-1}$		
Aq/nC_{60} large		0.75–1.5 $mg\ L^{-1}$		
PVP/C_{60}		0.6–1.0 $mg\ L^{-1}$		
0% Ag-MWCNTs	*Escherichia coli*	—	11.3	Hamouda *et al.*[54]
3% Ag-MWCNTs		—	14.8 ± 0.3	
6% Ag-MWCNTs		6 $\mu g\ mL^{-1}$	17.1 ± 0.1	
Ag NPs-PANI/MWCNT	*Escherichia coli*	—	≈18 mm	Deshmukh *et al.*[55]
Ag NPs on CNT carpets	*Escherichia coli*	—	No zone of inhibition	Karumuri *et al.*[56]

attributed to the ability of fullerenes to disrupt microbial cell membranes and generate ROS under certain conditions, which can damage cellular components irrespective of the bacterial cell wall structure. The findings herein, support the notion that the myriad and broad-spectrum mechanisms of action of fullerene derivatives, such as membrane disruption and ROS production, can be effective against both types of bacteria despite their structural differences. Furthermore, experimental conditions were optimized and consistent for both bacterial strains, ensuring reliable and comparable results.

These findings underscore the significant potential of metal-coordinated fullerenes in addressing the critical healthcare challenge of AMR. The rapid synthesis approach described herein offers a scalable and efficient method for producing these nanoparticles for industrial applications. The unique properties of fullerenes, combined with the synergistic effects observed in the metal-fullerene composites, present a versatile platform for developing novel antimicrobial agents that can surpass the limitations of conventional treatments. Similarly, the incorporation of fullerenes and Ag_3PO_4/Fe_3O_4 nanocomposite has been shown to significantly improve the antibacterial properties, where fullerene modified nanocomposite demonstrated biocidal activity.[46] Their ability to induce ROS, inhibit efflux pumps, and interact synergistically with metals positions them as potent candidates for combating resistant bacterial strains. Given the global rise of AMR and the dearth of new antibiotics, this research is both timely and crucial for safeguarding global public health.

The biological interactions and fate of nanomaterials are strongly influenced by their physical and chemical properties. Factors including size, shape, dissolution rate, chemical composition, surface energy, surface coating, and surface charge play a critical role in determining how these nanoparticles interact with biological systems. Additionally, the agglomeration state and crystal structure of nanoparticles influence their toxicity and therapeutic efficacy. Understanding these parameters is important in designing nanoparticles that achieve the desired biological outcomes, such as targeted drug delivery or minimizing adverse immune reactions.[47]

Metallic nanoparticles present promising opportunities for future nanomedicine due to their unique physicochemical properties, such as size, surface area, and surface energy, which enables them to interact with biological systems at the molecular level. These nanoparticles have the potential to be used as carriers for therapeutic agents, imaging agents, as well as direct therapeutics in cancer treatment, antimicrobial applications, and regenerative medicine. However, challenges remain, particularly their long-term stability, potential toxicity, carcinogenicity, teratogenicity and ability to evade the immune system. Additionally, developing scalable and cost-effective synthesis methods that maintain consistency and functionality is essential for their translation to clinical use. Addressing this kind of challenges could unlock the full potential of metallic nanoparticles in nanomedicine.[48]

Surface functionalization of nanoparticles is a critical process to enhances their performance and imparts unique properties, particularly in biomedical and nanomedicine applications. By modifying the surface of nanoparticles, it is possible to improve their solubility, stability, and interaction with biological systems, thus making them suitable for applications such as targeted drug delivery and diagnostics. Functionalized nanoparticles exhibit higher selectivity and reduced toxicity, which is essential for therapeutic applications. Previous studies have shown that chemical modifications significantly influence the interactions between fullerenes and proteins which may affect their antibacterial properties.[49] Furthermore, this process can introduce chemical groups or molecules that provide certain bindings to specific biological targets, thereby increase the efficacy of the nanoparticles in their designated roles. These advancements enable nanoparticles to be used in imaging, therapy, and as drug delivery systems.[50,51]

The obtained results in this study showed promising antimicrobial properties on both Gram-positive and Gram-negative bacteria using modified fullerenes nanocomposite compared with similar studies of carbon-based nanocomposites, as shown in Table 3.

Conclusions

In conclusion, this study highlights the broad-spectrum utility of functionalized silver-coordinated chloro-fullerenes and copper-coordinated chloro-fullerenes as a promising avenue for developing advanced antimicrobial agents.

Prospective investigations will also focus on further elucidating their mechanisms of action to fully leverage their therapeutic potential, including exploring their biocidal activity against a wider range of microbial species, including viruses, fungi, and other critical priority AMR bacterial stains described by World Health Organization (WHO) in the 2024 updated Bacterial Priority Pathogens List (BPPL).[52] Finally, with any new chemical entity, extensive biocompatibility and cytotoxicity evaluations are important. Future efforts will be directed at investigating Ag-C_{60}-Cl and Cu-C_{60}-Cl fullerenes *in vivo* and exploring the incorporation of other metals to better understand their potential in clinical application as a safe, alternative antimicrobial approach.

Abbreviations

AMR	Antimicrobial resistance
BPPL	Bacterial priority pathogens list
BHI	Brain heart infusion
Cu-C_{60}	Copper coordinated chloro-fullerenes nanoparticles
E. coli	*Escherichia coli*
EtBr	Ethidium bromide
C_{60}	Fullerenes
LB	Luria Bertani
MRSA	Methicillin-resistant *Staphylococcus aureus*
MIC	Minimum inhibitory concentrations
OD	Optical density
ROS	Reactive oxygen species

SEM-EDS	Scanning electron microscopy-energy dispersive X-ray spectrometer
Ag-C_{60}	Silver-coordinated chloro-fullerenes nanoparticles
XPS	X-ray photoelectron spectroscopy

Data availability

The data supporting this article have been included as part of the ESI.†

Author contributions

AI conceived the study, designed and performed the experiments, interpreted the results, and wrote the manuscript. TK designed, assisted with experiments and interpreted the results. KN performed SEM experiments for the nanoparticles. GP performed TEM experiments. JA performed and analyzed computational data. AI, ALD, DL, and SO conceived the study, designed the experiments, interpreted the results, and wrote the manuscript.

Conflicts of interest

There are no conflicts to declare.

Acknowledgements

This work was performed at the Joint School of Nanoscience and Nanoengineering, a member of the Southeastern Nanotechnology Infrastructure Corridor (SENIC) and National Nanotechnology Coordinated Infrastructure (NNCI), supported by the NSF (grant ECCS-1542174). The authors would like to acknowledge funding support from the National Science Foundation for funding of the AccelNet INFRAMES project, as well as the TUCASI Foundation. We are grateful for financial support from the DEVCOM Soldier Center and the UNC ROI program, and the NC Collaboratory. The authors would like to thank Dr Tetyana Ignatova for her valuable comments and edits on the experimental Raman results. The authors acknowledge the DOD HBCU/MSI instrumentation award (contract #: W911NF1910522) to acquire HR-TEM (JEOL 2100PLUS) with STEM/EDS capability.

Notes and references

1 C. J. L. Murray, K. S. Ikuta, F. Sharara, L. Swetschinski, G. Robles Aguilar, A. Gray, C. Han, C. Bisignano, P. Rao, E. Wool, S. C. Johnson, A. J. Browne, M. G. Chipeta, F. Fell, S. Hackett, G. Haines-Woodhouse, B. H. Kashef Hamadani, E. A. P. Kumaran, B. McManigal, S. Achalapong, R. Agarwal, S. Akech, S. Albertson, J. Amuasi, J. Andrews, A. Aravkin, E. Ashley, F.-X. Babin, F. Bailey, S. Baker, B. Basnyat, A. Bekker, R. Bender, J. A. Berkley, A. Bethou, J. Bielicki, S. Boonkasidecha, J. Bukosia, C. Carvalheiro, C. Castañeda-Orjuela, V. Chansamouth, S. Chaurasia, S. Chiurchiù, F. Chowdhury, R. Clotaire Donatien, A. J. Cook, B. Cooper, T. R. Cressey, E. Criollo-Mora, M. Cunningham, S. Darboe, N. P. J. Day, M. De Luca, K. Dokova, A. Dramowski, S. J. Dunachie, T. Duong Bich, T. Eckmanns, D. Eibach, A. Emami, N. Feasey, N. Fisher-Pearson, K. Forrest, C. Garcia, D. Garrett, P. Gastmeier, A. Z. Giref, R. C. Greer, V. Gupta, S. Haller, A. Haselbeck, S. I. Hay, M. Holm, S. Hopkins, Y. Hsia, K. C. Iregbu, J. Jacobs, D. Jarovsky, F. Javanmardi, A. W. J. Jenney, M. Khorana, S. Khusuwan, N. Kissoon, E. Kobeissi, T. Kostyanev, F. Krapp, R. Krumkamp, A. Kumar, H. H. Kyu, C. Lim, K. Lim, D. Limmathurotsakul, M. J. Loftus, M. Lunn, J. Ma, A. Manoharan, F. Marks, J. May, M. Mayxay, N. Mturi, T. Munera-Huertas, P. Musicha, L. A. Musila, M. M. Mussi-Pinhata, R. N. Naidu, T. Nakamura, R. Nanavati, S. Nangia, P. Newton, C. Ngoun, A. Novotney, D. Nwakanma, C. W. Obiero, T. J. Ochoa, A. Olivas-Martinez, P. Olliaro, E. Ooko, E. Ortiz-Brizuela, P. Ounchanum, G. D. Pak, J. L. Paredes, A. Y. Peleg, C. Perrone, T. Phe, K. Phommasone, N. Plakkal, A. Ponce-de-Leon, M. Raad, T. Ramdin, S. Rattanavong, A. Riddell, T. Roberts, J. V. Robotham, A. Roca, V. D. Rosenthal, K. E. Rudd, N. Russell, H. S. Sader, W. Saengchan, J. Schnall, J. A. G. Scott, S. Seekaew, M. Sharland, M. Shivamallappa, J. Sifuentes-Osornio, A. J. Simpson, N. Steenkeste, A. J. Stewardson, T. Stoeva, N. Tasak, A. Thaiprakong, G. Thwaites, C. Tigoi, C. Turner, P. Turner, H. R. Van Doorn, S. Velaphi, A. Vongpradith, M. Vongsouvath, H. Vu, T. Walsh, J. L. Walson, S. Waner, T. Wangrangsimakul, P. Wannapinij, T. Wozniak, T. E. M. W. Young Sharma, K. C. Yu, P. Zheng, B. Sartorius, A. D. Lopez, A. Stergachis, C. Moore, C. Dolecek and M. Naghavi, Global Burden of Bacterial Antimicrobial Resistance in 2019: A Systematic Analysis, *Lancet*, 2022, **399**(10325), 629–655, DOI: 10.1016/S0140-6736(21)02724-0.

2 Centers for Disease Control and Prevention (U.S.), *Antibiotic Resistance Threats in the United States, 2019*, Centers for Disease Control and Prevention, U.S., 2019, doi: DOI: 10.15620/cdc:82532.

3 C. L. Ventola, The Antibiotic Resistance Crisis: Part 1: Causes and Threats, *P T Peer-Rev. J. Formul. Manag.*, 2015, **40**(4), 277–283.

4 R. Y. Pelgrift and A. J. Friedman, Nanotechnology as a Therapeutic Tool to Combat Microbial Resistance, *Adv. Drug Delivery Rev.*, 2013, **65**(13–14), 1803–1815, DOI: 10.1016/j.addr.2013.07.011.

5 M. C. Teixeira; E. Sanchez-Lopez; M. Espina; A. C. Calpena; A. M. Silva; F. J. Veiga; M. L. Garcia; E. B. Souto Advances in Antibiotic Nanotherapy, in *Emerging Nanotechnologies in Immunology*; Elsevier, 2018, pp. 233–259, doi: DOI: 10.1016/B978-0-323-40016-9.00009-9.

6 L. Zhang, J. Xia, Q. Zhao, L. Liu and Z. Zhang, Functional Graphene Oxide as a Nanocarrier for Controlled Loading and Targeted Delivery of Mixed Anticancer Drugs, *Small*, 2010, **6**(4), 537–544, DOI: 10.1002/smll.200901680.

7 M. A. Bakht, M. J. Ansari, Y. Riadi, N. Ajmal, M. J. Ahsan and M. S. Yar, Physicochemical Characterization of

Benzalkonium Chloride and Urea Based Deep Eutectic Solvent (DES): A Novel Catalyst for the Efficient Synthesis of Isoxazolines under Ultrasonic Irradiation, *J. Mol. Liq.*, 2016, **224**, 1249–1255, DOI: **10.1016/j.molliq.2016.10.105**.

8 G. Benelli and C. M. Lukehart, Special Issue: Applications of Green-Synthesized Nanoparticles in Pharmacology, Parasitology and Entomology, *J. Cluster Sci.*, 2017, **28**(1), 1–2, DOI: **10.1007/s10876-017-1165-5**.

9 M. Javed Ansari, A. Soltani, M. Ramezanitaghartapeh, P. Singla, M. Aghaei, H. Khandan Fadafan, S. Ardalan Khales, M. Shariati, H. Shirzad-Aski, H. Balakheyli, S. Sarim Imam and A. Zafar, Improved Antibacterial Activity of Sulfasalazine Loaded Fullerene Derivative: Computational and Experimental Studies, *J. Mol. Liq.*, 2022, **348**, 118083, DOI: **10.1016/j.molliq.2021.118083**.

10 R. Bakry, R. M. Vallant, M. Najam-ul-Haq, M. Rainer, Z. Szabo, C. W. Huck and G. K. Bonn, Medicinal Applications of Fullerenes, *Int. J. Nanomed.*, 2007, **2**(4), 639–649, DOI: **10.2147/IJN.S2.4.639**.

11 L. L. Dugan, E. G. Lovett, K. L. Quick, J. Lotharius, T. T. Lin and K. L. O'Malley, Fullerene-Based Antioxidants and Neurodegenerative Disorders, *Parkinsonism Relat. Disord.*, 2001, **7**(3), 243–246, DOI: **10.1016/S1353-8020(00)00064-X**.

12 M. S. Misirkic, B. M. Todorovic-Markovic, L. M. Vucicevic, K. D. Janjetovic, V. R. Jokanovic, M. D. Dramicanin, Z. M. Markovic and V. S. Trajkovic, The Protection of Cells from Nitric Oxide-Mediated Apoptotic Death by Mechanochemically Synthesized Fullerene (C60) Nanoparticles, *Biomaterials*, 2009, **30**(12), 2319–2328, DOI: **10.1016/j.biomaterials.2009.01.023**.

13 A. Kumar, M. V. Rao and S. K. Menon, Photoinduced DNA Cleavage by Fullerene–Lysine Conjugate, *Tetrahedron Lett.*, 2009, **50**(47), 6526–6530, DOI: **10.1016/j.tetlet.2009.09.027**.

14 M. Kumar and K. Raza, C60-Fullerenes as Drug Delivery Carriers for Anticancer Agents: Promises and Hurdles, *Pharm. Nanotechnol.*, 2018, **5**(3), 169–179, DOI: **10.2174/2211738505666170301142232**.

15 A. F. De Faria, F. Perreault, E. Shaulsky, L. H. Arias Chavez and M. Elimelech, Antimicrobial Electrospun Biopolymer Nanofiber Mats Functionalized with Graphene Oxide–Silver Nanocomposites, *ACS Appl. Mater. Interfaces*, 2015, **7**(23), 12751–12759, DOI: **10.1021/acsami.5b01639**.

16 K. J. Moor, C. O. Osuji and J.-H. Kim, Dual-Functionality Fullerene and Silver Nanoparticle Antimicrobial Composites *via* Block Copolymer Templates, *ACS Appl. Mater. Interfaces*, 2016, **8**(49), 33583–33591, DOI: **10.1021/acsami.6b10674**.

17 P. K. Sudeep, B. I. Ipe, K. G. Thomas, M. V. George, S. Barazzouk, S. Hotchandani and P. V. Kamat, Fullerene-Functionalized Gold Nanoparticles. A Self-Assembled Photoactive Antenna-Metal Nanocore Assembly, *Nano Lett.*, 2002, **2**(1), 29–35, DOI: **10.1021/nl010073w**.

18 S. Mallik, A. S. Mohd, A. Koutsioubas, S. Mattauch, B. Satpati, T. Brückel and S. Bedanta, Tuning Spinterface Properties in Iron/Fullerene Thin Films, *Nanotechnology*, 2019, **30**(43), 435705, DOI: **10.1088/1361-6528/ab3554**.

19 L. Brunet, D. Y. Lyon, E. M. Hotze, P. J. J. Alvarez and M. R. Wiesner, Comparative Photoactivity and Antibacterial Properties of C_{60} Fullerenes and Titanium Dioxide Nanoparticles, *Environ. Sci. Technol.*, 2009, **43**(12), 4355–4360, DOI: **10.1021/es803093t**.

20 V. Krishna, D. Yanes, W. Imaram, A. Angerhofer, B. Koopman and B. Moudgil, Mechanism of Enhanced Photocatalysis with Polyhydroxy Fullerenes, *Appl. Catal., B*, 2008, **79**(4), 376–381, DOI: **10.1016/j.apcatb.2007.10.020**.

21 R. Kawasaki, D. Antoku, R. Ohdake, K. Sugikawa and A. Ikeda, Bacterial Elimination *via* the Photodynamic Activity of a Fullerene/Light-Harvesting Antenna Molecule Assembled System Integrated into Liposome Membranes, *Nanoscale Adv.*, 2020, **2**(10), 4395–4399, DOI: **10.1039/D0NA00132E**.

22 Harvard Medical School Electron Microscopy Core, *Methods* | *Electron Microscopy* | *Harvard Medical School*, Retrieved October 4, 2024, from, **https://electron-microscopy.hms.harvard.edu/methods**.

23 I. Wiegand, K. Hilpert and R. E. W. Hancock, Agar and Broth Dilution Methods to Determine the Minimal Inhibitory Concentration (MIC) of Antimicrobial Substances, *Nat. Protoc.*, 2008, **3**(2), 163–175, DOI: **10.1038/nprot.2007.521**.

24 D. V. Parikh, T. Fink, K. Rajasekharan, N. D. Sachinvala, A. P. S. Sawhney, T. A. Calamari and A. D. Parikh, Antimicrobial Silver/Sodium Carboxymethyl Cotton Dressings for Burn Wounds, *Text. Res. J.*, 2005, **75**(2), 134–138, DOI: **10.1177/004051750507500208**.

25 M. AlAfeefi, M. Al Numairy and A. Al Dhamin, Necrosis and Changes in Pigmentation Following Silver Nitrate Application: A Case Report, *Adv. Skin Wound Care.*, 2024, **37**(8), 1–2, DOI: **10.1097/ASW.0000000000000175**.

26 R. Kapukaya and O. Ciloglu, Treatment of Chronic Wounds with Polyurethane Sponges Impregnated with Boric Acid Particles: A Randomised Controlled Trial, *Int. Wound J.*, 2020, **17**(5), 1159–1165, DOI: **10.1111/iwj.13463**.

27 J. M. Pérez, I. L. Calderón, F. A. Arenas, D. E. Fuentes, G. A. Pradenas, E. L. Fuentes, J. M. Sandoval, M. E. Castro, A. O. Elías and C. C. Vásquez, Bacterial Toxicity of Potassium Tellurite: Unveiling an Ancient Enigma, *PLoS One*, 2007, **2**(2), e211, DOI: **10.1371/journal.pone.0000211**.

28 L. R. Christena, V. Mangalagowri, P. Pradheeba, K. B. A. Ahmed, B. I. S. Shalini, M. Vidyalakshmi, V. Anbazhagan and N. Sai Subramanian, Copper Nanoparticles as an Efflux Pump Inhibitor to Tackle Drug Resistant Bacteria, *RSC Adv.*, 2015, **5**(17), 12899–12909, DOI: **10.1039/C4RA15382K**.

29 Y. Hou, B. Nie and Z. Li, Raman Spectroscopy of $AgNO_3$ Complex Encapsulated Fullerene (C60) Microcube, *Vib. Spectrosc.*, 2020, **109**, 103089, DOI: **10.1016/j.vibspec.2020.103089**.

30 Y. Hou, Y. Pan, C. Dong and B. Nie, Direct Transformation of $AgNO_3$ Complex Encapsulated Fullerene (C_{60}) Microcrystal on Solid Silver Nitrate Crystal without Organic Ligands, *Appl. Organomet. Chem.*, 2020, **34**(12), e5978, DOI: **10.1002/aoc.5978**.

31 R. Manaila, A. Belu-Marian, D. Macovei, G. Brehm, D. Th. Marian and I. Baltog, Evidence for Metal-C60 Interface Interaction from Raman Spectroscopy, *J. Raman Spectrosc.*, 1999, **30**(11), 1019–1025, DOI: **10.1002/(SICI)1097-4555(199911)30:11<1019::AID-JRS437>3.0.CO;2-W**.

32 R. Kato and K. Miyazawa, Raman Laser Polymerization of C 60 Nanowhiskers, *J. Nanotechnol.*, 2012, **2012**, 1–6, DOI: **10.1155/2012/101243**.

33 M. V. P. Dos Santos, Y. G. Proenza, A. Mahmood and R. L. Longo, PICVib: An Accurate, Fast and Simple Procedure to Investigate Selected Vibrational Modes at High Theoretical Levels and Evaluate Raman Intensities: PICVib Approach for Raman Intensities, *J. Raman Spectrosc.*, 2017, **48**(2), 327–335, DOI: **10.1002/jrs.5008**.

34 A. D. Becke, A New Mixing of Hartree–Fock and Local Density-Functional Theories, *J. Chem. Phys.*, 1993, **98**(2), 1372–1377, DOI: **10.1063/1.464304**.

35 A. Hamdan and M. Korek, Spin-Orbit Electronic Structure of the ScBr Molecule, *J. Mod. Phys.*, 2011, **02**(10), 1172–1177, DOI: **10.4236/jmp.2011.210146**.

36 S. Grimme, S. Ehrlich and L. Goerigk, Effect of the Damping Function in Dispersion Corrected Density Functional Theory, *J. Comput. Chem.*, 2011, **32**(7), 1456–1465, DOI: **10.1002/jcc.21759**.

37 C. J. Villagómez, I. L. Garzón and L. O. Paz-Borbón, A First-Principles DFT Dispersion-Corrected C60/Au(111) Raman Study, *Comput. Mater. Sci.*, 2020, **171**, 109208, DOI: **10.1016/j.commatsci.2019.109208**.

38 K. Saeedfar, L. Heng, T. Ling and M. Rezayi, Potentiometric Urea Biosensor Based on an Immobilised Fullerene-Urease Bio-Conjugate, *Sensors*, 2013, **13**(12), 16851–16866, DOI: **10.3390/s131216851**.

39 B. Dong, S. Belkhair, M. Zaarour, L. Fisher, J. Verran, L. Tosheva, R. Retoux, J.-P. Gilson and S. Mintova, Silver Confined within Zeolite EMT Nanoparticles: Preparation and Antibacterial Properties, *Nanoscale*, 2014, **6**(18), 10859–10864, DOI: **10.1039/C4NR03169E**.

40 M. Martins, M. P. McCusker, M. Viveiros, I. Couto, S. Fanning, J.-M. Pagès and L. A. Amaral, Simple Method for Assessment of MDR Bacteria for Over-Expressed Efflux Pumps, *Open Microbiol. J.*, 2013, **7**(1), 72–82, DOI: **10.2174/1874285801307010072**.

41 A. Gaurav, P. Bakht, M. Saini, S. Pandey and R. Pathania, Role of Bacterial Efflux Pumps in Antibiotic Resistance, Virulence, and Strategies to Discover Novel Efflux Pump Inhibitors, *Microbiology*, 2023, **169**(5), 001333, DOI: **10.1099/mic.0.001333**.

42 H.-M. Zhang, J. Cao, B.-P. Tang and Y.-Q. Wang, Effect of TiO_2 Nanoparticles on the Structure and Activity of Catalase, *Chem.-Biol. Interact.*, 2014, **219**, 168–174, DOI: **10.1016/j.cbi.2014.06.005**.

43 A. Nandi, L.-J. Yan, C. K. Jana and N. Das, Role of Catalase in Oxidative Stress- and Age-Associated Degenerative Diseases, *Oxid. Med. Cell. Longevity*, 2019, **2019**, 1–19, DOI: **10.1155/2019/9613090**.

44 Y.-X. Pan, Q.-H. Xu, H.-M. Xiao and C.-Y. Li, Insights into the Antibacterial Activity and Antibacterial Mechanism of Silver Modified Fullerene towards Staphylococcus Aureus by Multiple Spectrometric Examinations, *Chemosphere*, 2023, **342**, 140136, DOI: **10.1016/j.chemosphere.2023.140136**.

45 O. Bolshakova, V. Lebedev, E. Mikhailova, O. Zherebyateva, L. Aznabaeva, V. Burdakov, Y. Kulvelis, N. Yevlampieva, A. Mironov, I. Miroshnichenko and S. Sarantseva, Fullerenes on a Nanodiamond Platform Demonstrate Antibacterial Activity with Low Cytotoxicity, *Pharmaceutics*, 2023, **15**(7), 1984, DOI: **10.3390/pharmaceutics15071984**.

46 S. Sepahvand and S. Farhadi, Fullerene-Modified Magnetic Silver Phosphate (Ag_3 PO_4/Fe_3 O_4/C_{60}) Nanocomposites: Hydrothermal Synthesis, Characterization and Study of Photocatalytic, Catalytic and Antibacterial Activities, *RSC Adv.*, 2018, **8**(18), 10124–10140, DOI: **10.1039/C8RA00069G**.

47 H. Samadian, M. S. Salami, M. Jaymand, A. Azarnezhad, M. Najafi, H. Barabadi and A. Ahmadi, Genotoxicity Assessment of Carbon-Based Nanomaterials; Have Their Unique Physicochemical Properties Made Them Double-Edged Swords?, *Mutat. Res.*, 2020, **783**, 108296, DOI: **10.1016/j.mrrev.2020.108296**.

48 D. Nayak; H. Chopra; I. Chakrabartty; M. Saravanan; H. Barabadi; Y. K. Mohanta Opportunities and Challenges for Bioengineered Metallic Nanoparticles as Future Nanomedicine, in *Bioengineered Nanomaterials for Wound Healing and Infection Control*, Elsevier, 2023, pp. 517–540. doi: DOI: **10.1016/B978-0-323-95376-4.00012-5**.

49 Y. Bai, X. Wu, P. Ouyang, M. Shi, Q. Li, T. Maimaiti, S. Lan, S.-T. Yang and X.-L. Chang, Surface Modification Mediates the Interaction between Fullerene and Lysozyme: Protein Structure and Antibacterial Activity, *Environ. Sci.: Nano*, 2021, **8**(1), 76–85, DOI: **10.1039/D0EN00645A**.

50 S. Majeed, M. Saravanan, M. Danish, N. A. Zakariya, M. N. M. Ibrahim, E. H. Rizvi, S. U. NisaAndrabi, H. Barabadi, Y. K. Mohanta and E. Mostafavi, Bioengineering of Green-Synthesized TAT Peptide-Functionalized Silver Nanoparticles for Apoptotic Cell-Death Mediated Therapy of Breast Adenocarcinoma, *Talanta*, 2023, **253**, 124026, DOI: **10.1016/j.talanta.2022.124026**.

51 H. Barabadi; H. Noqani; K. Jounaki; A. Nasiri; K. Karami; R. Jahani Functionalized Bioengineered Metal-Based Nanomaterials for Cancer Therapy, in *Functionalized Nanomaterials for Cancer Research*, Elsevier, 2024, pp. 219–260. doi: DOI: **10.1016/B978-0-443-15518-5.00024-0**.

52 WHO, *Bacterial Priority Pathogens List 2024 Bacterial Pathogens of Public Health Importance, to Guide Research, Development, and Strategies to Prevent and Control Antimicrobial Resistance*, World Health Organization, Geneva, 2024.

53 D. Y. Lyon, L. K. Adams, J. C. Falkner and P. J. J. Alvarez, Antibacterial Activity of Fullerene Water Suspensions: Effects of Preparation Method and Particle Size, *Environ. Sci. Technol.*, 2006, **40**(14), 4360–4366, DOI: **10.1021/es0603655**.

54 H. I. Hamouda, H. M. Abdel-Ghafar and M. H. H. Mahmoud, Multi-Walled Carbon Nanotubes Decorated with Silver Nanoparticles for Antimicrobial Applications, *J. Environ.*

Chem. Eng., 2021, **9**(2), 105034, DOI: 10.1016/j.jece.2021.105034.

55 S. P. Deshmukh, A. G. Dhodamani, S. M. Patil, S. B. Mullani, K. V. More and S. D. Delekar, Interfacially Interactive Ternary Silver-Supported Polyaniline/Multiwalled Carbon Nanotube Nanocomposites for Catalytic and Antibacterial Activity, *ACS Omega*, 2020, **5**(1), 219–227, DOI: 10.1021/acsomega.9b02526.

56 A. K. Karumuri, D. P. Oswal, H. A. Hostetler and S. M. Mukhopadhyay, Silver Nanoparticles Supported on Carbon Nanotube Carpets: Influence of Surface Functionalization, *Nanotechnology*, 2016, **27**(14), 145603, DOI: 10.1088/0957-4484/27/14/145603.